A Theory for the Seasonal Predictability Barrier: Threshold, Timing, and Intensity

ZHENGYU LIU

Atmospheric Science Program, Department of Geography, The Ohio State University, Columbus, Ohio

YISHUAI JIN

Department of Atmospheric and Oceanic Sciences, Peking University, Beijing, China

XINYAO RONG

State Key Laboratory of Severe Weather, Chinese Academy of Meteorological Sciences, Beijing, China

(Manuscript received 20 June 2018, in final form 1 October 2018)

ABSTRACT

A theory is developed in a stochastic climate model for understanding the general features of the seasonal predictability barrier (PB), which is characterized by a band of maximum decline in autocorrelation function phase-locked to a particular season. Our theory determines the forcing threshold, timing, and intensity of the seasonal PB as a function of the damping rate and seasonal forcing. A seasonal PB is found to be an intrinsic feature of a stochastic climate system forced by either seasonal growth rate or seasonal noise forcing. A PB is generated when the seasonal forcing, relative to the damping rate, exceeds a modest threshold. Once generated, all the PBs occur in the same calendar month, forming a seasonal PB. The PB season is determined by the decline of the seasonal forcing as well as the delayed response associated with damping. As such, for a realistic weak damping, the PB season is locked close to the minimum SST variance under the seasonal growth-rate forcing, but after the minimum SST variance under the seasonal noise forcing. The intensity of the PB is determined mainly by the amplitude of the seasonal forcing. The theory is able to explain the general features of the seasonal PB of the observed SST variability over the world. In the tropics, a seasonal PB is generated mainly by a strong seasonal growth rate, whereas in the extratropics a seasonal PB is generated mainly by a strong seasonal noise forcing. Our theory provides a general framework for the understanding of the seasonal PB of climate variability.

1. Introduction

A distinct seasonal predictability barrier (PB) has long been noticed in the tropical Pacific sea surface temperature (SST) variability and the associated El Niño–Southern Oscillation (ENSO) variability in rainfall (Walker and Bliss 1932; Wright 1979) and sea level pressure (Troup 1965; Webster and Yang 1992). This seasonal PB is characterized by a band of maximum decline in monthly autocorrelation function (ACF), sometimes also referred to as a persistence barrier (Troup 1965; Torrence and Webster 1998), at the fixed phase of May–June, and can be seen in the seasonal ACF of SST variability over the central–eastern Pacific (Fig. 1a; 95% significance level is 0.3 for 46 years of data) and its lag gradient (Fig. 1b) (e.g., Ren et al. 2016). This seasonal phase-locking of PB implies that, regardless of the initial month, a damped persistence forecast loses its predictability most rapidly in the following May, forming the so-called spring PB of ENSO. This barrier in persistence forecast also corresponds to a barrier of predictability in ensemble forecast (e.g., Levine and McPhaden 2015). Since the PB season occurs close to the time of minimum SST variance, it has often been interpreted as caused by the minimum SST variance in spring (left panel of Fig. 1a), when the weak ENSO signal renders it most vulnerable to noise forcing and, in turn, a transition from one climate state to another (e.g., Webster and Yang 1992; Xue et al. 1994; Torrence and Webster 1998; Boschat et al. 2013; Levine and McPhaden 2015; Tasambay-Salazar et al. 2015; Ren et al. 2016; Moon and Wettlaufer 2017). Recent studies have also found similar seasonal PB in other

Denotes content that is immediately available upon publication as open access.

Corresponding author: Zhengyu Liu, liu.7022@osu.edu; jinyishuai@126.com

DOI: 10.1175/JCLI-D-18-0383.1

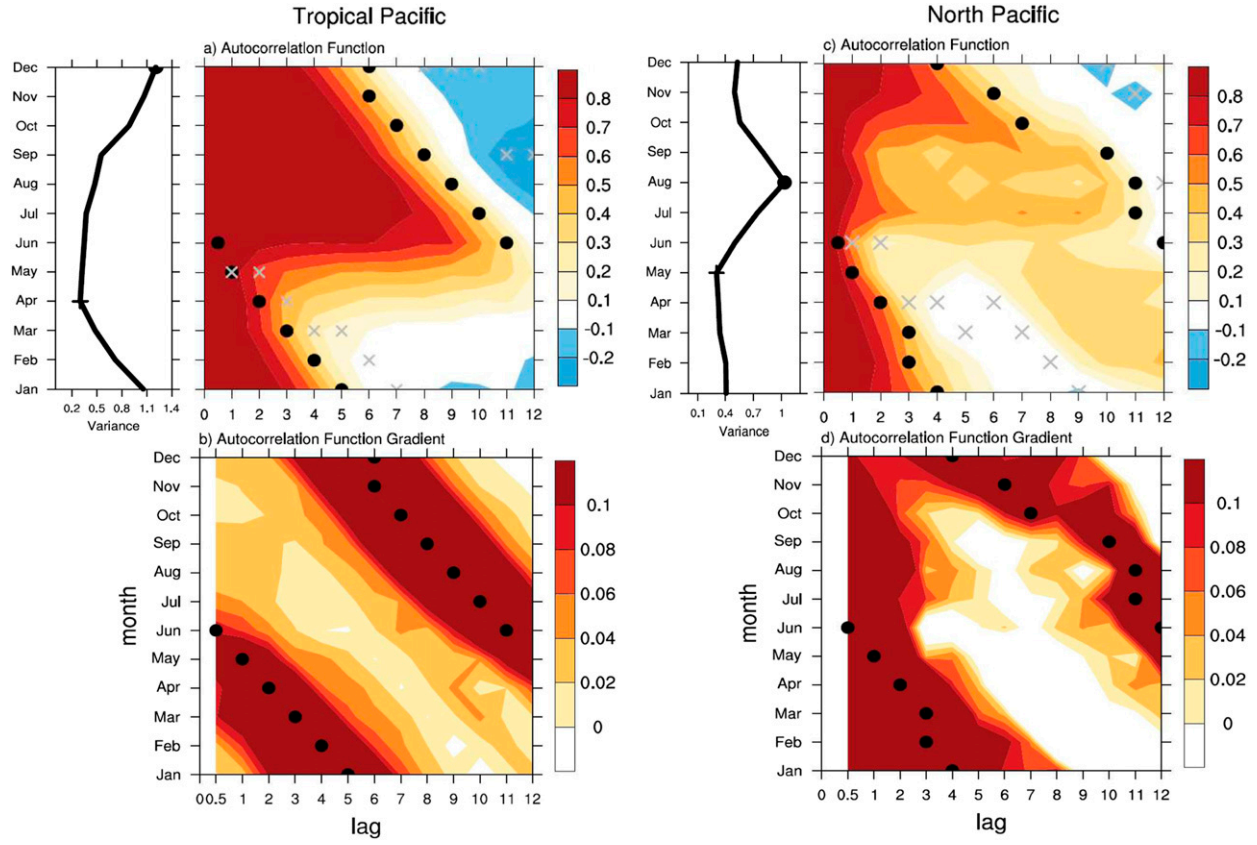

FIG. 1. (a) Seasonal cycle of SST (left) variance [black; $(°C)^2$; solid circle for maximum and plus sign for minimum] and (right) autocorrelation function (ACF) $[r(t, \tau)]$ in the tropical Pacific (Niño-3.4 region, 5°S–5°N, 170°–120°W) calculated directly from the monthly SST anomaly in the observation (appendix C). The black filled circles on the ACF map mark the month of maximum ACF decline, or predictability barrier (PB). (b) The corresponding lag gradient of the ACF (month^{-1}) $-r_\tau(t, \tau)$. (c),(d) As in (a) and (b), but for the North Pacific reemergence region (38°–42°N, 160°E–180°). Gray crosses in (a) and (c) mark the month of minimum ACF (minimum persistence).

regions, for example, the western North Pacific in the so-called reemergence region (38°–42°N, 160°E–180°; Alexander et al. 1999), where SST variability also exhibits a band of maximum ACF decline phase-locked to June, or the so-called summer PB in the North Pacific (Figs. 1c,d) (Zhao et al. 2012). Since the SST variability in the North Pacific and tropical Pacific is generated predominantly by different mechanisms (the former by climate noise, the latter by ocean–atmosphere feedback), it is interesting that a similar seasonal PB is generated in both regions, implying some general mechanism for the generation of seasonal PB. Meanwhile, in contrast to the tropical Pacific where the PB month is locked close to, and is therefore interpreted as generated by, the minimum SST variance, the summer PB in the North Pacific occurs between the minimum and maximum SST variances, the latter of which occurs in late summer due to the shallow mixed layer (e.g., Zhao et al. 2012). This suggests that the seasonal PB in the North Pacific, unlike the tropical Pacific, may not be generated simply by the minimum SST variance.

Here, we study the seasonal PB in the framework of the simplest stochastic climate model: the Langevin equation (Hasselmann 1976), with the incorporation of a seasonal cycle in the damping rate and noise forcing. In the discrete form, this seasonal stochastic model corresponds to the first-order autoregressive (AR1) model with periodic coefficients and the analysis in this system is referred to as the cyclostationary analysis (Bennett 1958; Hurd 1975). ENSO PB has been studied extensively in the discrete AR1 model (Torrence and Webster 1998; Ren et al. 2016), as well as the continuous models of the Langevin model (Moon and Wettlaufer 2017) and delayed oscillator models (Stein et al. 2010; Levine and McPhaden 2015). These studies have shown the existence of the seasonal PB and discussed its responses to some model parameters. Nevertheless, the solutions so far are either derived numerically or expressed in rather complex forms (e.g., Torrence and Webster 1998; Levine and McPhaden 2015) such that important questions on the seasonal SB in general still remain not fully

understood. In particular, we are interested in three questions regarding the condition, timing, and intensity of the seasonal PB. First, what is the necessary forcing condition for a seasonal PB? Second, what determines the timing and intensity of a seasonal PB? Third, are there other regions in the World Ocean where seasonal PB is present and, if yes, why they are present?

This paper is an attempt to understand the general features of the seasonal PB with the focus on the three questions raised above. In particular, we will derive a general, albeit asymptotic, solution of the seasonal Langevin equation. This solution will enable us to develop a theory for the necessary forcing condition, the timing, and the intensity of the seasonal PB, shedding light on the mechanism of seasonal PB. We will also apply our theory to assess the seasonal PB in the SST variability observations over the world. We will show that seasonal PB is a general feature of a seasonal stochastic model once the seasonal forcing, either in growth rate or in noise forcing, exceeds a modest threshold. The timing of a PB depends on the damping rate of the system as well as the type and magnitude of the seasonal forcing, while the intensity of a PB depends on the magnitude of the seasonal forcing. Our theory is found to be able to explain some major features of the seasonal PBs in the observed SST variability over the world.

The paper is organized as follows. The seasonal stochastic climate model is introduced in section 2 and a general solution is derived for the necessary forcing condition, the timing, and the intensity of the seasonal PB. The seasonal PB is then studied in the idealized cases forced by the seasonal growth rate and noise forcing in sections 3 and 4, respectively. The theory is applied to the observed SST variability in the tropical and North Pacific in section 5 and for the World Ocean in section 6. Section 7 presents the conclusions and some discussions. In a companion paper (Y. Jin et al. 2018, unpublished manuscript), we study in detail another feature of the phase-locking: the phase-locking of the SST variance and its relation with the lag-1 persistence.

2. General solution for seasonal predictability barrier

We will develop the theory in the Langevin equation (Hasselmann 1976), instead of the cyclostationary AR1 model (e.g., Torrence and Webster 1998), because the former allows us to derive a simple analytical solution for seasonal PB, shedding light on the mechanism of the seasonal PB. The Langevin equation that incorporates a seasonal cycle in the growth rate and noise forcing can be written as

$$\frac{dT}{dt} + b(t)T = N(t), \tag{2.1}$$

where T is the SST anomaly. The damping rate $b(t)$, or growth rate $-b(t)$, has an annual mean magnitude b_0, annual frequency ω, and a relative amplitude A as

$$b(t) = b_0[1 - A\cos(\omega t)]. \tag{2.2}$$

The stochastic forcing is a white noise of zero mean, with a variance of annual mean magnitude σ_0^2 and a seasonal amplitude D (<1):

$$\langle N(t), N(t')\rangle = \sigma_N^2(t)\delta(t-t') \quad \text{and}$$
$$\sigma_N^2(t) = \sigma_0^2[1 + D\cos(\omega t - \beta)], \tag{2.3}$$

where the angle brackets denote the ensemble covariance. The phase of the seasonal cycle here is chosen such that month $t = 0$ corresponds to the month of maximum growth rate $-b$, and it leads the month of maximum noise intensity $\sigma_N^2(t)$ by β. The purpose of the rest of this section is to derive a general solution for the seasonal ACF and, then, the seasonal PB. The application of the solution will be left to later sections.

In general, the ACF of the seasonal Langevin equations [(2.1)–(2.3)] can be derived in the integral form. Given the general solution of SST variability to (2.1) as

$$T(t) = \int_{-\infty}^{t} \exp\left[-\int_s^t b(u)\,du\right] N(s)\,ds,$$

the lagged autocovariance function can be derived as

$$\begin{aligned} C(t,\tau) \equiv \langle T(t), T(t+\tau)\rangle &= \left\langle \int_{-\infty}^{t} \exp\left[-\int_s^t b(u)\,du\right] N(s)\,ds, \int_{-\infty}^{t+\tau} \exp\left[-\int_q^{t+\tau} b(v)\,dv\right] N(q)\,dq \right\rangle \\ &= \int_{-\infty}^{t} \exp\left[-\int_s^t b(u)\,du\right] \int_{-\infty}^{t+\tau} \exp\left[-\int_q^{t+\tau} b(v)\,dv\right] \langle N(s), N(q)\rangle\,ds dq \\ &= \sigma_0^2 \exp\left(-B\omega\left(t+\frac{\tau}{2}\right) + \frac{AB}{2}\{\sin(\omega t) + \sin[\omega(t+\tau)]\}\right) \int_{-\infty}^{t} \exp[B\omega s - AB\sin(\omega s)][1 + D\cos(\omega s - \beta)]\,ds, \end{aligned} \tag{2.4}$$

where

$$B = \frac{2b_0}{\omega} \tag{2.5}$$

is the damping rate normalized by the annual frequency and its value ranges from 0.2 to 1.5 for the SST variability in observations (see Fig. 8a). The SST variance $\sigma_T^2(t) \equiv C(t, 0)$ is therefore

$$\sigma_T^2(t) = \sigma_0^2 \exp[-B\omega t + AB\sin(\omega t)] \int_{-\infty}^{t} \exp[B\omega s - AB\sin(\omega s)][1 + D\cos(\omega s - \beta)]\, ds. \tag{2.6}$$

The lagged autocorrelation function can be derived from (2.4) and (2.6) as

$$r(t,\tau) = \frac{C(t,\tau)}{\sigma_T(t)\sigma_T(t+\tau)} = \exp\left(-\frac{B}{2}\omega\tau - \frac{B^2 A}{2}\{\sin(\omega t) - \sin[\omega(t+\tau)]\}\right) \times \frac{\sigma_T(t)}{\sigma_T(t+\tau)}, \tag{2.7}$$

where (2.6) can be integrated numerically such that (2.6) and (2.7) give the full solution to the Langevin equation in the integral form.

To shed light on the mechanism of PB, we derive asymptotic solutions. In the limit of weak seasonal cycle of growth rate,

$$AB \ll 1, \tag{2.8}$$

we have $\exp[-AB\sin(\omega s)] \approx 1 - AB\sin(\omega s)$, the variance integral (2.6) can be integrated analytically at the leading order as

$$\sigma_T^2(t) \approx \frac{\sigma_0^2}{2b_0}\left[1 + \frac{BM'}{\sqrt{1+B^2}}\cos(\omega t - \theta_1 - \theta_2)\right], \tag{2.9}$$

where the phase of variance response is

$$\theta_1 = \arcsin\left(\frac{1}{\sqrt{1+B^2}}\right), \tag{2.10}$$

with $0 \le \theta_1 \le \pi/2$, and

$$\theta_2 = \arcsin\left(\frac{D\sin\beta}{M'}\right), \tag{2.11}$$

with $M' = \sqrt{A^2 + D^2 + 2AD\cos\beta}$. Since the minimum variance has often been used for the interpretation of PB in previous works (e.g., Webster and Yang 1992; Xue et al. 1994; Torrence and Webster 1998; Levine and McPhaden 2015; Ren et al. 2016), we denote the month of minimum variance from (2.9) as

$$\omega t_V = \theta_1 + \theta_2 - \pi. \tag{2.12}$$

If we further assume a weak seasonal cycle of the noise forcing

$$DB \ll 1, \tag{2.13}$$

the seasonal ACF can be derived from (2.7) and (2.9) at the leading order as

$$r(t,\tau) \approx \exp(-b_0\tau)\left[1 + \frac{BM}{\sqrt{1+B^2}}\sin\left(\frac{\omega\tau}{2}\right) \times \cos\left(\omega t + \frac{\omega}{2}\tau - \theta_1 - \theta_3\right)\right], \tag{2.14a}$$

where

$$\theta_3 = \arcsin\left(\frac{D\cos\beta}{M}\right) \tag{2.14b}$$

and

$$M = \sqrt{(AB)^2 + D^2 - 2ABD\sin\beta}. \tag{2.14c}$$

Here, M is the effective amplitude of the seasonal cycle of the combined growth rate and noise forcing. It reduces to the amplitude of the seasonal growth rate $M = AB$ in the absence of seasonal noise forcing ($D = 0$) and reduces to the amplitude of the seasonal noise forcing $M = D$ in the absence of seasonal growth rate ($A = 0$).[1]

Further asymptotic solution for PB can be derived for the lag derivatives on the ACF if we further assume a weak damping

$$B \ll 1. \tag{2.15}$$

At the leading order, the first and second derivatives of the ACF (2.13) reduce to, respectively,

$$\partial_\tau r(t,\tau) \approx -b_0 e^{-b_0\tau}\left[1 - \frac{M}{\sqrt{1+B^2}}\cos(\omega t + \omega\tau - \theta_1 - \theta_3)\right] \tag{2.16}$$

and

$$\partial_{\tau\tau} r(t,\tau) \approx b_0^2 e^{-b_0\tau}\left[1 - \frac{2M}{B}\cos(\omega t + \omega\tau - 2\theta_1 - \theta_3)\right]. \tag{2.17}$$

[1] The effective amplitude M also depends on the phase difference between noise and growth rate forcings β. The seasonal cycles of growth rate and noise forcing reinforce each other toward $\beta = -\pi/2$, whereas they cancel each other toward $\beta = \pi/2$.

A maximum decline in ACF occurs at[2]

$$\partial_{\tau\tau} r(t,\tau) \sim 1 - \frac{2M}{B}\cos(\omega t + \omega\tau - 2\theta_1 - \theta_3) = 0. \quad (2.18)$$

Therefore, the necessary forcing condition for a maximum ACF decline, or PB, is

$$M/B > 1/2. \quad (2.19)$$

That is, a PB emerges when the seasonal cycle amplitude M relative to the damping rate B exceeds a threshold of 1/2. Once (2.19) is satisfied, the PB exists throughout the year and remains on the fixed phase

$$\omega t + \omega\tau - 2\theta_1 - \theta_3 = \theta_4, \quad (2.20)$$

where

$$\theta_4 = \arccos(B/2M), \quad (2.21)$$

with $0 \le \theta_4 \le \pi/2$. Thus, a damped persistent forecast with its PB occurring at lag τ corresponds to the initial forecast month of

$$\omega t_B(\tau) = \omega t_{B_0} - \omega\tau, \quad (2.22)$$

where

$$\omega t_{B_0} = 2\theta_1 + \theta_3 + \theta_4. \quad (2.23)$$

Equation (2.22) shows that all the PBs form a phase line, along which the increase of the forecast lag $\omega\tau$ is compensated by the decrease of the calendar month ωt_B exactly. As such, all the PBs occurs on the same calendar month ωt_{B_0}, which will be defined as the PB month hereafter. It is this phase locking of the PB month that allows all the PBs to form the so-called seasonal PB: that is, regardless of the initial forecast month, the PB occurs at the same calendar month ωt_{B_0}. This seasonal PB phase line has been seen in the observations where the PB month ωt_{B_0} occurs in late spring and early summer in the tropical Pacific (Figs. 1a,b) and North Pacific (Figs. 1c,d), respectively.

The PB solution above shows two interesting features. First, the forcing magnitude has to exceed a threshold to generate a PB, and second, the PB, once generated, occurs on the same calendar month, forming a seasonal PB. The forcing threshold (2.19) is not surprising, although, to our knowledge, a threshold has not been derived and discussed in the literature. Without a seasonal cycle ($M = 0$), the ACF r and, in turn, its decline $|\partial_\tau r|$ decrease with lag monotonically at the damping rate $\sim Be^{-B\tau}$ as shown in (2.16), which has the maximum ACF decline always at the initial lag $\tau = 0$ and decreases monotonically with lag. Seasonal forcing obviously will lead to a seasonal modulation of the ACF decline, as in previous studies (e.g., Bennett 1958; Hurd 1975; Torrence and Webster 1998; Ren et al. 2016; Moon and Wettlaufer 2017). This will lead to a seasonal cycle, and therefore an increase and a decrease in $|\partial_\tau r|$ alternatively every other half year, relative to $Be^{-B\tau}$. The ACF decline $|\partial_\tau r|$, however, can remain monotonic if the seasonal cycle is too weak to distort the overall monotonic decline associated with the mean damping rate in $Be^{-B\tau}$. When the seasonal forcing is sufficiently strong [i.e., $M/B > 1/2$ as in (2.19)], obviously, it will be able to overwhelm the mean damping rate, and the change of ACF decline will no longer be monotonic. This generates a maximum ACF decline or PB. Second, and most interestingly, it is not obvious at all that the PB, once generated, has to be phase-locked to the same calendar month and then form a seasonal PB. Our analytical solution demonstrates, therefore, that the phase-locking of PB, or seasonal PB, is an intrinsic feature of the seasonal stochastic system: once maximum ACF decline is generated, it occurs along the same calendar month ωt_{B_0} in (2.23). It should be noted that, different from the maximum ACF decline that exhibits phase-locking, the minimum ACF, which is sometimes also referred to as a type of seasonal PB (e.g., Torrence and Webster 1998), is not phase-locked, a point to be returned to later (also see appendix A for more details).

The intensity of the seasonal PB can be measured by the magnitude of the maximum ACF decline. The instantaneous PB intensity at each lag can be calculated by substituting (2.22) and (2.10) into (2.16) as

$$|\partial_\tau r[t(\tau),\tau]|_B = b_0 S_B e^{-b_0\tau}, \quad (2.24)$$

where

$$S_B = \int_0^\infty |\partial_\tau r|_B \, d\tau = 1 + \frac{M}{1+B^2}\sqrt{1 - \left(\frac{B}{2M}\right)^2} - \frac{B^2}{2(1+B^2)} \quad (2.25)$$

is the PB intensity integrated over all the lags, which will be called the total intensity. The PB intensity over the first year, which is used sometimes in practice, can be calculated as

[2] PB is the extreme persistence decline $|\partial_\tau r|$ in the interior $\tau > 0$, which, during certain seasons, is smaller than the absolute maximum of persistence decline at the boundary $\tau = 0$.

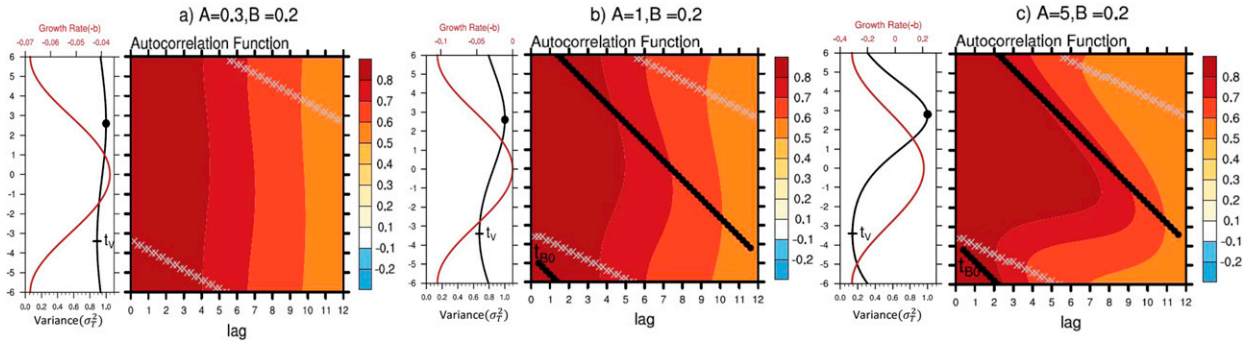

FIG. 2. As in Fig. 1, but for the full solution of the seasonal Langevin equation ($B = 0.2$) forced by the seasonal growth rates of (a) $A = 0.3$, (b) $A = 1$, and (c) $A = 5$. For each panel, (left) the seasonal cycle of the growth rate (brown) and the forced SST variance (black), with the maximum and minimum variance of the full solution marked by solid circle and plus, (right) the seasonal ACF with the black dots marking the months of maximum ACF declines and gray crosses marking the minimum ACF, or minimum persistence.

$$S_{B_1} = \int_0^{2\pi/\omega} |\partial_\tau r|_B \, d\tau = S_B(1 - e^{-B\pi}). \tag{2.26}$$

Therefore, the total intensity S_B increases mainly with the amplitude of the seasonal cycle forcing M, while the first year intensity S_{B_1} also decreases with the damping rate B.

It should be noted that caution should be taken on the application of the leading-order solutions of the PB to more general cases, notably the forcing threshold (2.19), the PB month (2.22), and intensity (2.25). Formally, these asymptotic solutions are valid in the limit of weak damping $B \ll 1$ in (2.15), which is sufficient to ensure $AB \ll 1$ in (2.8) and $DB \ll 1$ in (2.13). Nevertheless, there are also hints that these PB features may still be largely valid beyond the weak damping limit to the realistic range of B, up to ~1. First, these features can also be shown to be largely valid in an intermediate asymptotic solution (not shown), which uses the approximate ACF (2.14a) but calculates the gradients numerically, instead of using (2.16) and (2.17). This intermediate solution only requires $AB \ll 1$ and $DB \ll 1$, instead of $B \ll 1$. Second, these features seem to be also reasonably valid in the full solution of the Langevin Eq. (2.1) that is derived all numerically (see appendix B; see also Figs. 2, 4, and 7).

3. Seasonal predictability barrier forced by seasonal growth rate

We first examine the PB forced by the seasonal growth rate ($A > 0$) in the absence of seasonal noise variation ($D = 0$), such that $M = AB$, $\theta_2 = \theta_3 = 0$, in (2.11), (2.14b), and (2.14c). The forcing threshold (2.19) is reduced to

$$A \geq 1/2. \tag{3.1}$$

Now, the threshold is independent of B because of the cancelation of two opposite effects of the damping rate on PB: a larger B increases the damping, which is unfavorable for a PB, but also increases the amplitude of the seasonal cycle forcing ($=AB$), which is favorable for a PB. Following (2.22), the PB month is reduced to

$$\omega t_{B_0} = 2\theta_1 + \theta_4, \tag{3.2}$$

where

$$\theta_4 = \arccos(1/2A). \tag{3.3}$$

The month of minimum variance in (2.12) is reduced to

$$\omega t_V = \theta - \pi. \tag{3.4}$$

The variance now lags the growth rate by θ_1, and this lag increases from 0 at the strong damping limit to one season $\pi/2$ at the weak damping limit according to (2.8). A comparison of (3.2) and (3.4) shows that, in general, the PB month differs from the minimum variance month as

$$\omega t_{B_0} - \omega t_V = \theta_1 + \theta_4 - \pi. \tag{3.5}$$

In addition to the dependence on A (in θ_4), the phase difference between ωt_{B_0} and ωt_V also depends heavily on B (in θ) because ωt_{B_0} increases with θ_1 twice the rate of ωt_V.

Some general features of the PB month can be seen in three examples in the ACF maps in Fig. 2 (and more examples in Figs. B1a and B2a), which are obtained from the full solution (2.6) and (2.7) numerically, in the case of a weak damping $B = 0.2$ and in turn $\theta_1 \to \pi/2$. For a weak seasonal cycle below the forcing threshold ($A = 0.3$; Fig. 2a), no PB is generated and the magnitude of the ACF decline decreases monotonically with lag. When A increases above the threshold

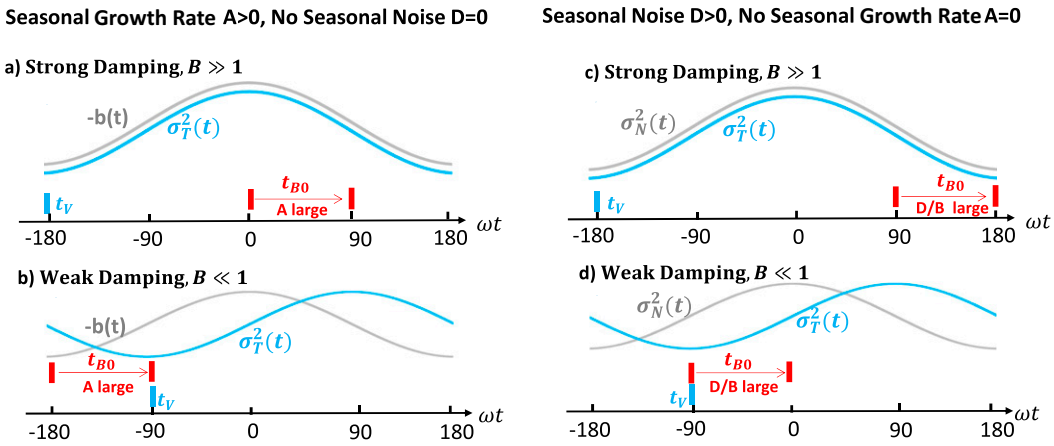

FIG. 3. Schematic figure showing the phase response of the SST variance $\sigma_T^2(t)$ (cyan), the minimum variance month t_V (cyan tick mark), and the range of PB month t_{B_0} (red tick mark) of increasing forcing. (a),(b) The strong and weak damping cases, respectively, forced by the seasonal growth rate (gray); (c),(d) the strong and weak damping cases, respectively, forced by the seasonal noise forcing (gray).

($A = 1$), a PB emerges with the PB locked to month of $\omega t_{B_0} \approx -4.5$ months (black circles, Fig. 2b). This PB month leads the minimum variance ($\omega t_V = -3.4$ months) by ~ -1.1 months, consistent with the asymptotic solution (3.5). When the seasonal cycle is further increased to $A = 5$ (Fig. 2c), ωt_{B_0} (≈ -3.8 months) approaches ωt_V as suggested in (3.5), because now $\theta_4 \to \pi/2$ in (3.3).

The general feature of the PB timing can be understood from two limiting cases as shown schematically in Figs. 3a and 3b. For a strong damping, the SST response to the growth rate is instantaneous, so that the variance is locked in phase with the growth rate such that $\theta_1 \to 0$. The PB month is then locked to the first season of growth rate declining (from the maximum to the annual mean): $0 < \omega t_{B_0} = \theta_4 < \pi/2$, and this phase θ_4 increases from 0 to $\pi/2$ when A increases from the threshold amplitude 1/2 to $A \gg 1$, according to (3.2) (Fig. 2a). Intuitively, the seasonal PB can be understood as caused by the rapid decline of the growth rate, which leads to the maximum decline in SST signal and, in turn, the ACF. Equation (3.5) shows that ωt_B differs from ωt_V more than $\pi/2$. As the damping rate diminishes ($B \ll 1$; Fig. 2b), the SST response lags the growth rate forcing by a season $\theta_1 \to \pi/2$, which delays the variance minimum by one season according to (3.4) but delays the PB month by two seasons according to (3.2). As such, the PB month is shifted close to the minimum variance within one season. If, additionally, the seasonal cycle is also strong ($A \gg 1$), (3.3) gives $\theta_4 \to \pi/2$, and therefore the PB month approaches the minimum variance $\omega t_{B_0} \to \omega t_V = -\pi/2$. This is the case of the example discussed in Fig. 2c. This turns out to be also the case for the spring PB of tropical Pacific in the observation, as will be discussed later in section 5. This analysis shows that the line-up of PB and minimum variance is generally not true. Instead, a PB is forced directly by the declining of the growth rate, and, in the meantime, is delayed by the damping rate, such that it approaches the minimum variance only in the limit of weak damping and strong seasonal growth rate forcing. It should be noted that the discussion above of the strong damping case (Fig. 3a) should be taken with caution, because our solution can be derived formally in the limit of weak damping. Nevertheless, the tendency from strong to weak damping discussed above still seems reasonable, at least, qualitatively. Partly, this is because our asymptotic solution seems qualitatively valid up to the modest damping regime $B \sim 1$ (as shown in Figs. B1 and B2).

Finally, the total intensity of the PB can be derived in the limit of weak damping $B \ll 1$ from (2.25) as

$$S_B \approx 1 + AB\sqrt{1 - (2A)^{-2}}. \tag{3.6}$$

Therefore, the PB intensifies mainly with the amplitude of the seasonal cycle AB. This can be seen in the more distinct PB bands in the examples shown in Figs. 2a–c, with increasing A and, in turn, AB. The increased PB intensity with A can also be seen more clearly in the examples in Fig. B2b.

4. Seasonal predictability barrier forced by seasonal noise forcing

We now study the effect of seasonal noise forcing ($D > 0$) in the absence of seasonal growth rate ($A = 0$), such that, from (2.11), (2.14b), and (2.14c),

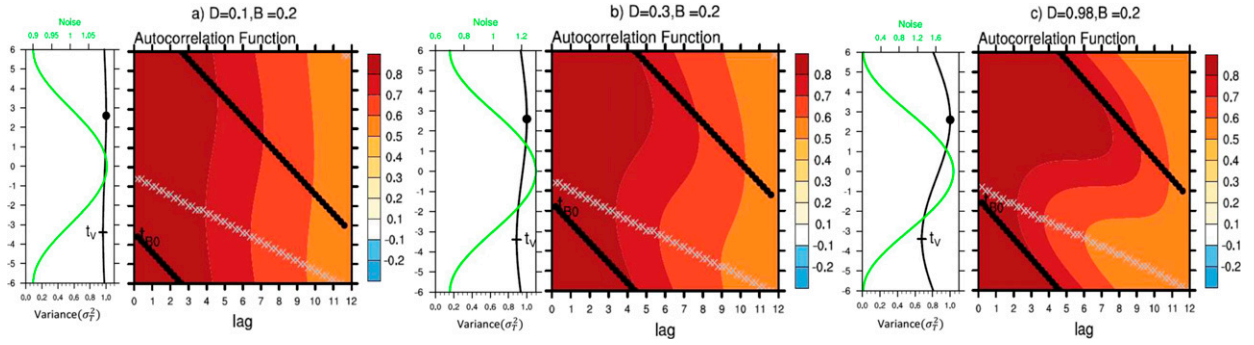

FIG. 4. As in Fig. 2, but for the cases of seasonal noise forcing of amplitude (green curve in the left panel) for (a) $D = 0.1$, (b) $D = 0.3$, and (c) $D = 0.98$, all with the damping rate $B = 0.2$.

$$M = D, \quad \theta_2 = 0, \quad \theta_3 = \pi/2,$$

where, for simplicity, we have set $\beta = 0$. Now, the forcing threshold (2.19) is reduced to

$$D/B \geq 1/2. \tag{4.1}$$

For a weak damping, PB band emerges as long as D exceeds a small damping-dependent threshold $B/2$. The PB month (2.23) is reduced to

$$\omega t_{B_0} = 2\theta_1 + \frac{\pi}{2} + \theta_4, \tag{4.2}$$

where

$$\theta_4 = \arccos(B/2D). \tag{4.3}$$

The minimum variance month remains the same as (3.4) and therefore, again, in general, the timings of PB and minimum variance differ as

$$\omega t_{B_0} - \omega t_V = \theta_1 + \theta_4 - \pi/2. \tag{4.4}$$

Some features of the PB month can be seen in three examples of weak damping rate ($B = 0.2$) in the full solution in Fig. 4 (also Figs. B1b and B2c). For a weak seasonal forcing ($D = 0.1$) that just exceeds the threshold (Fig. 4a), a PB emerges at the calendar month $\omega t_{B_0} = -3.4$ months; this phase almost coincides with ωt_V, because now $\theta_4 \to 0$. As D increases to 0.3 and, furthermore, to 0.98 (Figs. 4b,c), $\theta_4 \to \pi/2$, and therefore ωt_{B_0} lags ωt_V by one season, or between the minimum and maximum variance, as suggested by (4.4) (as in Fig. 3d hereafter).

General features of the PB can be discussed schematically as in Figs. 3c and 3d. For strong damping, $\theta_1 \to 0$ (Fig. 3c), the instantaneous SST response leads to the in-phase response of the SST variance and noise forcing. The PB month occurs at $\omega t_{B_0} = \pi/2 + \theta_4$. Similar to the case of seasonal growth rate forcing, the PB month also occurs during the declining stage of the noise forcing. The PB can therefore still be understood as generated by the declining forcing, the resulting maximum decline in the SST signal, and, eventually, its persistence. Different from the case of growth rate forcing when the PB occurs in the first season of declining growth rate (from the maximum to annual mean); however, the PB month occurs in the second season of declining growth rate (from the annual mean to the minimum forcing). This delay to the second season occurs because the noise forcing acts not only as the force to generate SST signal and, in turn, persistence, but also as the noise to destroy the persistence. In the case of a weak damping (Fig. 3d), however, the SST response, and therefore the minimum variance, is delayed by a season relative to the forcing, while the PB month is delayed by two seasons. Furthermore, with a large forcing D/B, we have $\theta_4 \to \pi/2$. Therefore, the PB month lags the minimum variance by a season in (4.4), or between the minimum and maximum variance. This turns out to be the case of the North Pacific summer PB, as will be discussed later in section 5. As in the case of seasonal growth rate forcing (Fig. 3a), the discussion of the strong damping case (Fig. 3c) should be treated with some caution, because our solution is valid formally only for weak damping.

Finally, from (2.25), the total intensity of PB can be derived as

$$S_B = 1 + D\sqrt{1 - (B/2D)^{-2}}. \tag{4.5}$$

Again, PB intensity increases with the amplitude of the seasonal forcing. Therefore, the PB intensity increases with D from Fig. 4a to Fig. 4c (also see examples in Fig. B2d). Some previous work on seasonal PB tend to use the SST variance, and the related signal-to-noise ratio, to explain the PB (e.g., Xue et al. 1994; Torrence

and Webster 1998). In contrast, here, we interpret the PB, the SST variance as well as their relationships all as the direct response to the seasonal forcing in the unified framework of a linear stochastic climate model. Our study shows that the relation between PB month and minimum variance is different between the growth rate forcing and noise forcing.

In the examples in Figs. 2 and 4, we also plotted the minimum ACF, or minimum persistence (gray crosses). It is interesting that the minimum persistence differs dramatically from the seasonal PB. First, the minimum persistence is not phase-locked to the same calendar month, because the lag increases twice the rate of the initial forecast month. Second, the initial month of minimum persistence differs from the PB month, but approaches the PB month for weak damping and strong seasonal cycle forcing. Finally, the minimum persistence is always present, with no threshold on the forcing, even in the case of very weak seasonal growth rate in Fig. 2a. These features are also present in the observation in the tropical Pacific and North Pacific (Figs. 1a,c) and will be discussed in more details in appendix A.

5. Application to tropical Pacific and North Pacific SSTs

Now, we apply the theory to the observed SST variability in the tropical Pacific and North Pacific, which have been briefly discussed earlier in Fig. 1. The monthly SST data are the Hadley Centre Sea Ice and Sea Surface Temperature dataset (HadISST) from 1960 to 2005 (Rayner et al. 2003). The SST anomaly is derived after subtracting the climatological seasonal cycle and linear trend. The ACF is constructed using two models (see appendix C for details). The first is the discrete cyclostationary AR1 model (e.g., Hasselmann and Barnett 1981; Ruiz de Elvira and Lemke 1982; Torrence and Webster 1998), in which the lag-1 coefficient is proportional to the growth rate. The 12-month seasonal cycles of SST variance, growth rate, and noise variance are calculated from the observation and the seasonal ACF is calculated using the AR1 model solution (appendix C). The second model is the seasonal Langevin equation [(2.1)] with the model parameters estimated from the observational SST; the model solution is then obtained numerically in the time step of 1 month (appendix C). The two approaches are complementary. The AR1 model, which has been used extensively in the past, captures the full variability of the original SST time series, but cannot be assessed against our theory quantitatively. The stochastic climate model can be assessed against our theory quantitatively, but loses high harmonics of SST variance. Here, we reexamine the seasonal PB in the tropical Pacific and North Pacific shown in Fig. 1, leaving the discussion to the World Ocean to the next section.

The tropical Pacific has a weak damping ($B \sim 0.2$, corresponding to $\theta_1 = 0.44\pi$). The growth rate exhibits a strong seasonal cycle ($A = 4$, brown curve in the left panels of Figs. 5a,d) and the growth rate becomes unstable from June to November with the peak in September, consistent with previous works (e.g., Moon and Wettlaufer 2017). Physically, the seasonal cycle of the growth rate can be understood from the coupled ocean–atmosphere instability in terms of the BJ index (Jin et al. 2006). Here, however, we only focus on the generation mechanism of the spring PB. The spring PB is forced predominantly by the growth rate. This can be seen in sensitivity experiments forced by the seasonal growth rate (Figs. 5a,d), noise forcing (Figs. 5b,e), and combined growth rate and noise forcing (Figs. 5c,f) in both the AR1 (Figs. 5a–c) and stochastic climate (Figs. 5d–f) models (see appendix C for details). A comparison of the SST variance (black curve in the left panel of each figure) of different forcing scenarios shows clearly the overwhelming role of the seasonal growth rate forcing, consistent with previous works (e.g., Torrence and Webster 1998; Levine and McPhaden 2015). The seasonal growth rate also forces the distinct spring PB (black dots), as seen in the similar ACF forced by the growth rate (Figs. 5a,d) and the combined forcing (Figs. 5c,f) and the observation (Fig. 1a). This PB is caused by the large amplitude of seasonal cycle $A = 4$, which well exceeds the forcing threshold of 1/2 as shown in (3.1). The PB month leads the minimum variance slightly, both lagging the minimum growth rate by about a season, consistent with the theory in the limit of weak damping and strong seasonal cycle (Fig. 3b). This coincidence of the timings of the PB and minimum variance has been interpreted as the weak ENSO signal rendering itself most vulnerable to noise forcing (e.g., Webster and Yang 1992; Xue et al. 1994; Torrence and Webster 1998; Levine and McPhaden 2015). However, as discussed in section 3, the PB month does not have to be locked with the minimum variance in general. Instead, our stochastic climate model offers an alternative explanation. The spring PB of ENSO is forced by the rapid decline of the growth rate late in the fall, which forces a rapid decline of the SST signal and, in turn, its persistence; the persistence decline is then delayed by the weakly damped response and the strong seasonal cycle, such that the PB month approaches the month of minimum variance, forming the spring PB. The PB month coincides with the minimum variance here because of the weak damping and strong seasonal growth rate.

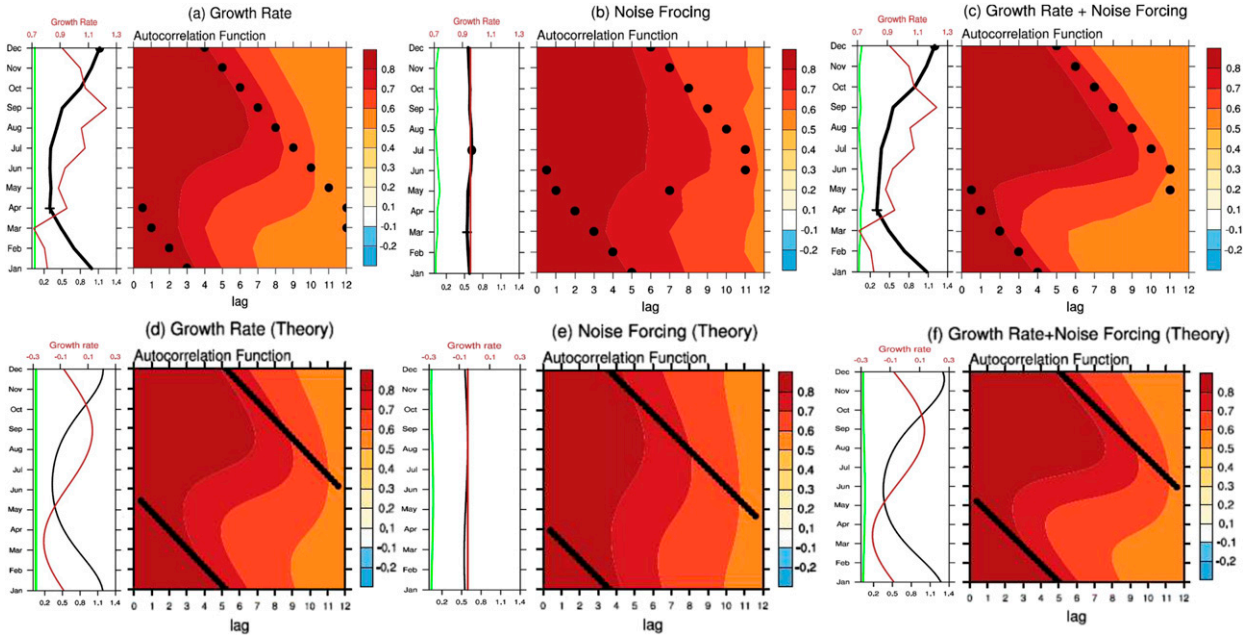

FIG. 5. SST variance and ACF map reconstructed using (a)–(c) the cyclostationary AR1 model solution and (d)–(f) the stochastic climate model solution, with the models derived from the observed SST variability in the tropical Pacific (in Fig. 1a). SST variability is forced by (a),(d) the seasonal growth rate, (b),(e) seasonal noise forcing, and (c),(f) the combined seasonal growth rate and noise forcing. In each panel, (left) the total SST variance (black), growth rate (brown), and noise forcing variance (green); (right) the seasonal ACF, with the PB marked by black dots.

It should be noted that both models, although capturing the PB timing in the observation, underestimate the PB intensity substantially (Figs. 5c,f vs Fig. 1a). It has been suggested that the intensity of the spring PB of ENSO can be enhanced by state-dependent noise. The main source of the noise is the wind bursts in the western to central equatorial Pacific, which may act as state-dependent noise for ENSO because their generation is enhanced by increased SSTs and associated convection (Levine and McPhaden 2015). Here, this underestimation is also contributed significantly by the deficiency of the AR1 model and the Langevin model, which fail to represent the oscillatory feature of ENSO, a point to be returned to later.

In contrast to ENSO, the summer PB in the North Pacific SST is forced by the seasonal noise forcing (Fig. 6). This is not surprising because the seasonal growth rate is much weaker ($A = 0.3$), and the seasonal noise forcing is much stronger ($D = 0.91$) than in the tropical Pacific. As a result, both the SST variance and ACF forced by the noise forcing (Figs. 6b,e) almost reproduce those by the combined forcing (Figs. 6c,f) and in the observation (Fig. 1c). Now, the damping rate is somewhat strong $B = 0.8$ (corresponding to $\theta_1 = 0.2\pi$) and thus SST variance lags the noise forcing by about 1.5 months. The PB month now straddles between the minimum and maximum SST variances, consistent with the discussion regarding Fig. 3d. The summer PB season is therefore caused by the strong noise forcing D in summer. Since the noise forcing (2.3) in our model (2.1) represents the effective noise forcing, which is proportional to the atmospheric noise forcing divided by the heat capacity of the ocean. Physically, this maximum D in summer is caused mainly by the shallower mixed layer, instead of the atmospheric variability itself (Zhao et al. 2012). Therefore, the summer PB in the western North Pacific can be understood as forced first by the declining noise forcing from summer toward the fall and then a delayed response time. The seasonal growth rate is too weak to force a PB by itself (Figs. 6a,d), because $A = 0.3$ is below the forcing threshold 1/2. Overall, the major features of the seasonal PB are consistent with our theory in both the tropical and North Pacific.

6. Application to the World Ocean

We now extend the application of our theory to the SST variability over the world. We will compare five analyses of seasonal PB, in which the ACFs are constructed by five methods: the direct observation calculation, the AR1 model solution, the AR2 model simulation, and the full and approximate solutions of the seasonal Langevin equation (appendix C). The direct observational analysis provides the benchmark that includes the full variability and dynamics. The AR1 model is used as the

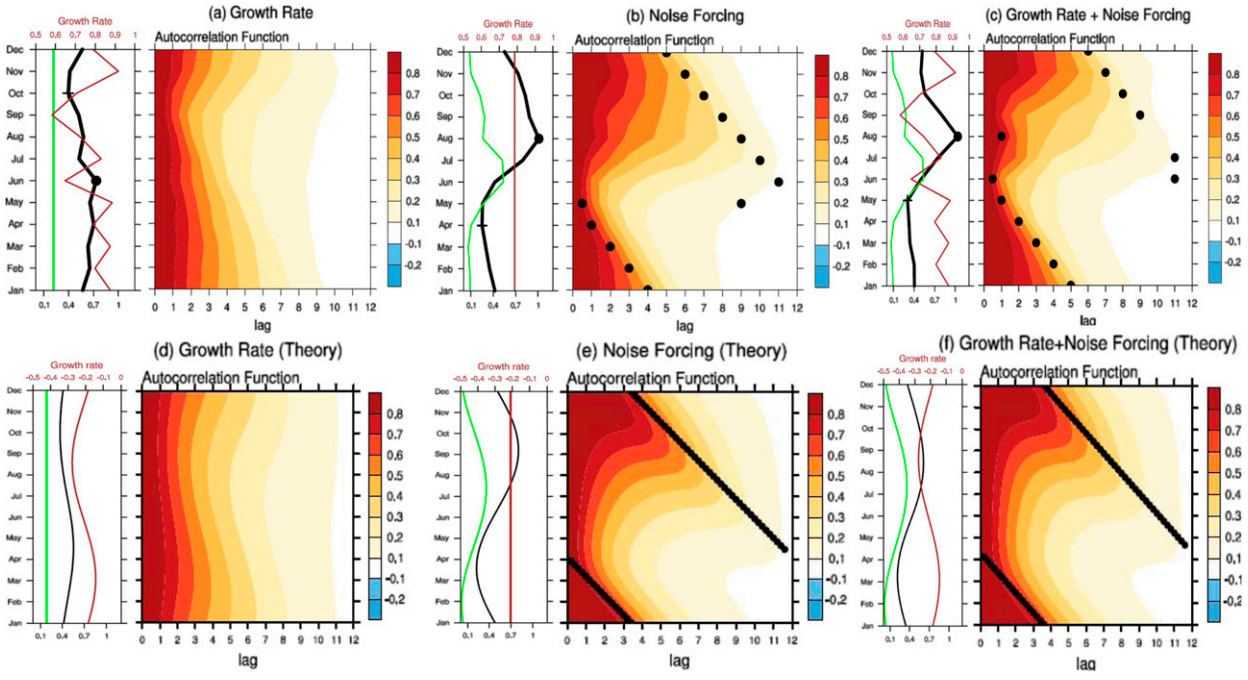

FIG. 6. As in Fig. 5, but for the western North Pacific in Fig. 1c.

simplest linear stochastic model to capture the full variability, while the AR2 model is a further improvement of the AR1 model with the inclusion of oscillatory variability. The full and approximate solutions of the Langevin equation are to test our theory against the observation for the annual harmonic variance.

At each grid box, five ACFs are constructed from the monthly SST anomalies using the five methods discussed above (see appendix C for details). Given a reconstructed ACF of $r(t, \tau)$, we analyze the seasonal PB of the 12 lags of the first year ($\tau = 1, 2, \ldots, 12$) as follows. First, for a calendar month t, we identify the lag of PB $\tau_B(t)$ at the lag of maximum ACF decline, which is calculated as the lag-gradient in the time step of 1 month as

$$s_B(t) = \left\{\frac{r[t, \tau_B(t) - 1] - r[t, \tau_B(t) + 1]}{2}\right\} = \max_\tau \left\{\frac{r(t, \tau - 1) - r(t, \tau + 1)}{2}\right\}, \quad (6.1)$$

where $s_B(t)$ is the maximum gradient. The corresponding PB month is estimated along the constant phase following (2.20) or (2.22) and (2.23) as

$$t_{B_0}(t) = t + \tau_B(t). \quad (6.2)$$

Note that, in a general analysis of the observation, it is a prior unknown if a seasonal PB exists or not, and therefore the 12 estimated $t_{B_0}(t)$ values may not be the same. The presence of a seasonal PB is therefore judged by the standard deviation of the 12 PB months as

$$\sigma_B = \sqrt{\frac{1}{11}\sum_{t=1}^{12}[t_{B_0}(t) - \bar{t}_{B_0}]^2}, \quad (6.3)$$

with the PB month estimated as the mean:

$$\bar{t}_{B_0} = \frac{1}{12}\sum_{t=1}^{12} t_{B_0}(t). \quad (6.4)$$

If $\sigma_B \ll 1$, the 12 estimated PB months are almost identical, and this should correspond to a sharp seasonal PB of month $\bar{t}_{B_0}$. In general, the smaller σ_B, the sharper the seasonal PB is. So, a small σ_B can serve as an upper bound criterion for judging the presence of a seasonal PB, such as the spring PB in the tropical Pacific ($\sigma_B = 0.52$, $\bar{t}_{B_0} = 5.5$; Fig. 1a) and summer PB in the North Pacific ($\sigma_B = 0.9$, $\bar{t}_{B_0} = 5.6$; Fig. 1c).

The intensity of the PB is estimated with the first year PB intensity (2.26) as

$$S_{B_1} = \sum_{t=1}^{12} s_B(t). \quad (6.5)$$

The tropical Pacific and North Pacific both have rather strong PB, with $S_{B_1} = 2.9$ and 2.6, respectively.

To assess the PB over the World Ocean, we calculate in Fig. 7 the PB intensity S_{B_1} (left column), the PB month

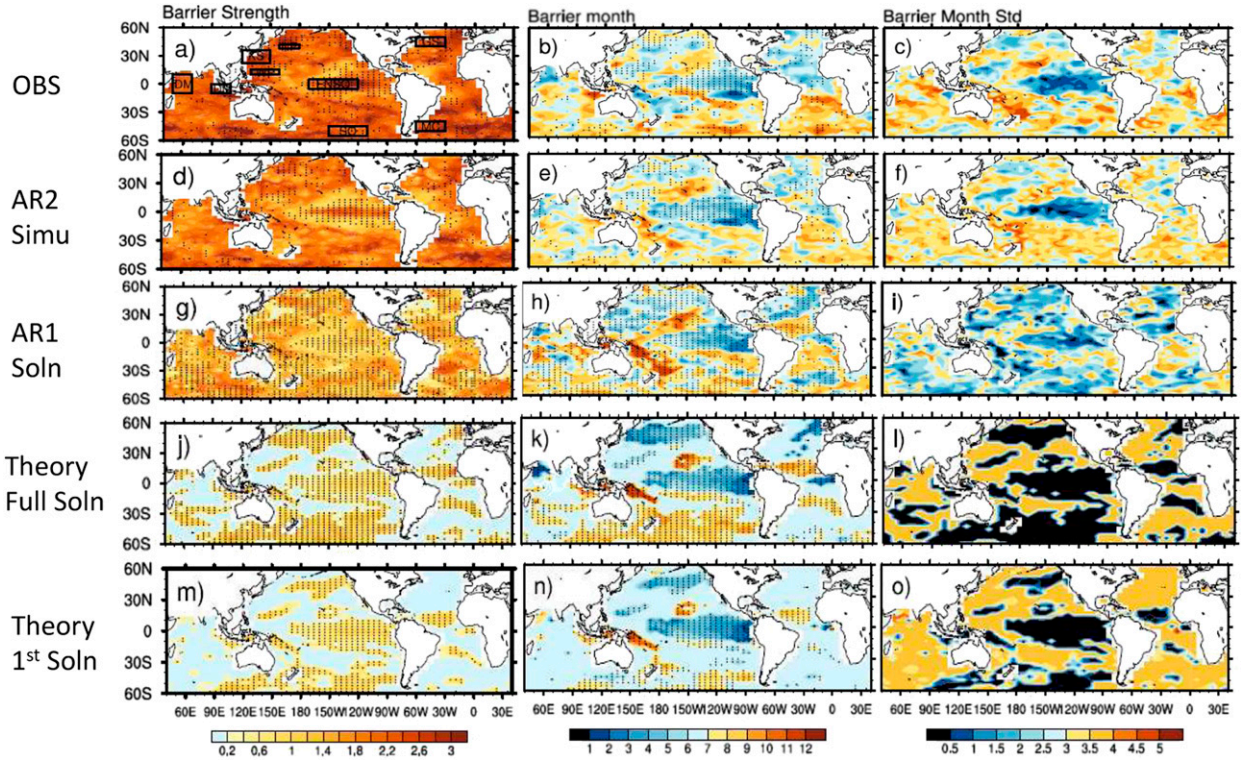

FIG. 7. (left) First-year PB intensity S_{B_1}, (center) mean PB month $\bar{t}_B$, and (right) standard deviation of PB month σ_B for monthly SST variability over the World Ocean assessed from the ACF map in each grid box (5.6° lon × 2.8° lat), for (a)–(c) observation, (d)–(f) AR2 model simulation, (g)–(i) AR1 model solution, and (j)–(l) full and (m)–(o) leading-order solutions of the stochastic climate model, respectively. Dots in the left and center columns mark the region of $\sigma_B < 2.5$ months, where a seasonal PB is likely present. The major feature is a similarity of the global seasonal PB pattern between various models and the observation.

mean $\bar{t}_{B_0}$ (center column), and the standard deviation σ_B (right column) of the 45 years of monthly SST variability over the world, with the ACF constructed directly from the observation (Figs. 7a–c), the AR1 solution (Figs. 7g–i), and the AR2 simulation (Figs. 7d–f). We will use $\sigma_B \leq 2.5$ as the criterion for a seasonal PB in the standard deviation maps (Figs. 7c,f,i), and the PB regions $\sigma_B < 2.5$ are marked in dots in the intensity and timing maps of the corresponding SST (Figs. 7a,b,d,e,g,h).

Major features of the seasonal PB over the world show strong similarity between the observation (Figs. 7a–c) and the AR1 model (Figs. 7g–i). In both analyses, first, the region of the sharpest seasonal PB occurs in the tropical Pacific (around the ENSO region marked in Fig. 7a), with the entire region of $\sigma_B < 1$–2 (Figs. 7c,i). The PB month (Figs. 7b,h) occurs from April to July in the equatorial region, consistent with the spring PB of ENSO discussed earlier, and shifts to earlier spring south of the equator. Second, the midlatitude North Pacific (around the NP region marked in Fig. 7a) also exhibits seasonal PB with $\sigma_B < 2$ (Figs. 7c,i), and PB month in early summer (Figs. 7b,h), again consistent with discussions in section 5. Third, there are additional regions of seasonal PB, such as the summer PB in the western tropical North Pacific (around the WP region marked in Fig. 7a), and the austral summer PB in the Southern Ocean (around the SO region marked in Fig. 7a). There are also regions that show no indication of seasonal PB, such as the western boundary regions of the Kuroshio, the Gulf Stream, and the Malvinas Current (around the regions of KS, GS, and MC, respectively, in Fig. 7a), all of large spread $\sigma_B > 3$.

In comparison with the observation, the AR1 model also shows a PB intensity of a similar spatial pattern, but with an overall weaker magnitude (within the dotted regions; cf. Figs. 7g and 7a). This underestimation of PB intensity has been seen in the ENSO region discussed earlier in Fig. 5. One reason of the weaker PB in the AR1 model is its inability to simulate the oscillatory evolution features in the observation. This is confirmed by the AR2 model simulation, which indeed shows a much enhanced PB intensity (Fig. 7d), now comparable with the observation (Fig. 7a), while the standard deviation and mean of the PB month (Figs. 7e,f) remain similar to the observation and the AR1 model.

The major features of the seasonal PB discussed above are also captured by the full solution of the stochastic climate model (Figs. 7j–l), in both the PB region (of small σ_B in Fig. 7l) and PB month (Fig. 7k), notably the spring PB over the tropical Pacific, the summer PB over the midlatitude North Pacific, and the austral summer PB over the Southern Ocean. Relative to the observation and AR models, however, the theory shows much sharper seasonal PB, characterized by much smaller σ_B ($\sigma_B < 0.5$). The difference between the theory and the AR1 model solution suggests that the seasonal PB is also distorted by higher annual harmonics in the AR1 model. Indeed, our theory applies to any harmonic ω after the effective damping is scaled as $B = 2b_0/\omega$. A higher harmonic has a larger ω and, in turn, a smaller B, lowering the forcing threshold for the noise forcing, as shown in (4.1). These higher harmonics can therefore distort the seasonal PB established by the annual harmonics in the AR models. Furthermore, the lack of higher harmonics also leads to an underestimation of the PB intensity in the theory (Fig. 7j) than in the AR1 solution (Fig. 7g). In the meantime, the overall larger σ_B in the AR1 model (Fig. 7i) than in the Langevin equation (Fig. 7l) over the PB region indicates that higher harmonics also distort the presence of a sharp PB phase line.

Finally, major PB features identified in the full solution of the Langevin equation (Figs. 7j–l) are well approximated in the asymptotic solution (Figs. 7m–o). The PB intensity and month are almost identical (Figs. 7j,k vs Figs. 7m,n). The PB regions are also very consistent in the maps of larger σ_B (cf. Figs. 7l and 7o), although the asymptotic solution underestimates the region of PB somewhat in the extratropics where B is large. This underestimation is caused by the overestimation of the forcing threshold (4.1) in the asymptotic solution under the seasonal noise forcing, as discussed in appendix B (see Fig. B1b). Overall, however, in spite of the formal assumptions of weak seasonal cycle in (2.8) and (2.13) and the weak damping in (2.15), the asymptotic solution is able to capture the major features of the full solution in the realistic regime of model parameters.

Given the success of the asymptotic solution, we can interpret the seasonal PB in the observation using the asymptotic solution in terms of the damping rate and seasonal forcing as shown in Fig. 8. Figure 8e shows the theoretical forcing threshold $M/2B$ in (2.19). It is seen that the regions of seasonal PB discussed before, such as the tropical Pacific, midlatitude and western tropical North Pacific, and the Southern Ocean, are indeed consistent with the threshold of $M/2B > 1$. Furthermore, this threshold is reached mainly by the large seasonal cycle amplitude M. The large amplitude is contributed

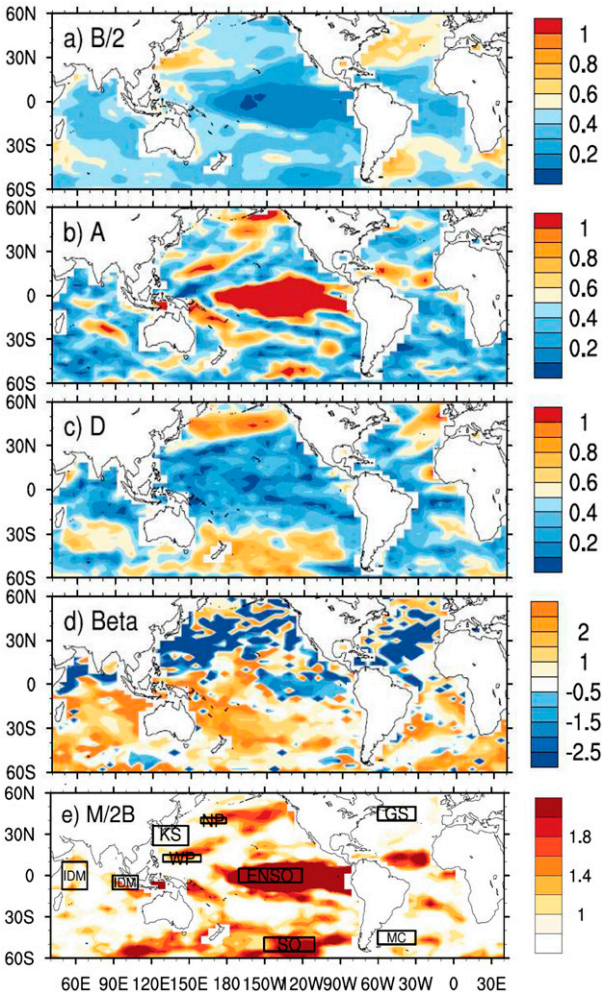

FIG. 8. Fitting forcing parameters for the annual harmonic of SST variability of the World Ocean in the stochastic climate model: (a) damping parameter $B/2$, (b) amplitude of seasonal growth rate A, (c) amplitude of seasonal noise forcing D, (d) phase difference between seasonal growth rate and noise forcing β, and (e) effective amplitude of seasonal forcing $M/2B$.

predominantly by the seasonal growth rate $A > 1/2$ in the tropical Pacific (Fig. 8b) but the seasonal noise forcing $D > B/2$ in the extratropics (cf. Figs. 8c and 8a).

We now discuss six regional PBs in more details as for the tropical and North Pacific in section 5. The domains and the corresponding model parameters of these regions, along with the tropical and North Pacific regions, are listed in Table 1, with domains also marked in Figs. 7a and 8e. The model parameters and the presence of PB for each region are also summarized in appendix B (Fig. B1, cyan circles). The western tropical North Pacific (WP; 10°–15°N, 130°–160°E) shows a sharp PB in June in the observation ($\sigma_B = 1.5$, $\bar{t}_{B_0} = 6.4$, $S_{B_1} = 2.7$) as seen clearly in the ACF calculated directly from the observation (Fig. 9a). The generation of the PB

TABLE 1. Model parameters for the eight regions. The 95% significance levels are shown in parentheses for A, B, and D. The significance level is calculated with the Monte Carlo method with 1000 simulations, each using a random Gaussian error of the same variance replacing the residual of the annual harmonic fitting.

	Domain	A	B	D	β	σ_B	$\bar{t}_{B_0}$	S_{B_1}
Tropical Pacific (TP)	5°S–5°N, 170°–120°W	4 (0.34, 8.39)	0.2 (0.03,0.34)	0.28 (0.1, 0.67)	−108°	0.52	5.5	2.9
North Pacific (NP)	38°–42°N, 160°E –180°	0.3 (0.14, 0.76)	0.8 (0.57, 1.1)	0.91 (0.41, 1.42)	97°	0.9	5.6	2.6
Western tropical North Pacific (WP)	10°–15°N, 130°–160°E	0.86 (0.44, 1.3)	0.73 (0.53, 0.87)	0.37 (0.27, 0.48)	−151°	1.5	6.4	2.7
Southern Ocean (SO)	45°–55°S, 150°–110°W	1 (0.28, 1.8)	0.46 (0.53, 0.87)	0.76 (0.27, 0.48)	40°	0.51	11.1	2.1
Indian Ocean Dipole (IDM) (E–W)	E: 10°S–10°N, 50°–70°E; W: 10°–0°S, 90°–110°W	0.92 (0.38, 1.3)	0.73 (0.65, 1.14)	0.15 (0.01, 0.57)	−60°	3.5	3.5	2.7
Kuroshio (KS)	22°–36°N, 122°–150°E	0.68 (0.15, 1.19)	1.24 (0.84, 1.63)	0.32 (0.22, 0.56)	116°	3.8	7.4	3.1
Gulf Stream (GS)	40°–50°N, 60°–30°W	0.58 (0.16, 1.0)	1.08 (0.76, 1.37)	0.5 (0.17, 0.82)	99°	3.8	6.7	2.6
Malvinas Current (MC)	40°–50°S, 60°–30°W	0.27 (0.07, 0.62)	1.5 (1.14, 1.86)	0.39 (0.22, 0.56)	59°	3.8	7.8	2.6

can be understood in theory from the forcing parameters ($B = 0.73$, $A = 0.86$, $D = 0.37$, $\beta = -151°$) and individually forced solutions (not shown). Both the theory and the experiments show that the noise forcing forces a PB in April while the growth rate and the combined forcing force a PB in June as in the observation (Fig. 9a). Thus, the summer PB is dominated by the growth rate forcing. The Southern Ocean in the Pacific sector (SO; 45°–55°S, 150°–110°W) also exhibits a clear PB, now in austral summer from November to December ($\sigma_B = 0.51$, $\bar{t}_{B_0} = 11.1$, $S_{B_1} = 2.1$). Theoretical forcing parameters ($B = 0.46$, $A = 1$, $D = 0.76$, $\beta = 40°$) and individually forced solutions (not shown) show that the growth rate forces a PB in June while the noise forcing and the combined forcing force a PB in November similar to the observation (Fig. 9b). Thus, the occurrence of PB in austral summer can be understood as the dominance of the local noise forcing, whose maximum is caused mainly by the shallow mixed layer in local summer, as in the North Pacific discussed before (Zhao et al. 2012). The PB analysis can also be applied to a climate index with seasonal phase-locking, such as the Indian Ocean dipole mode (IDM), which is defined as the SST difference between the eastern (10°S–10°N, 50°–70°E) and western (10°S–0°, 90°–110°W)

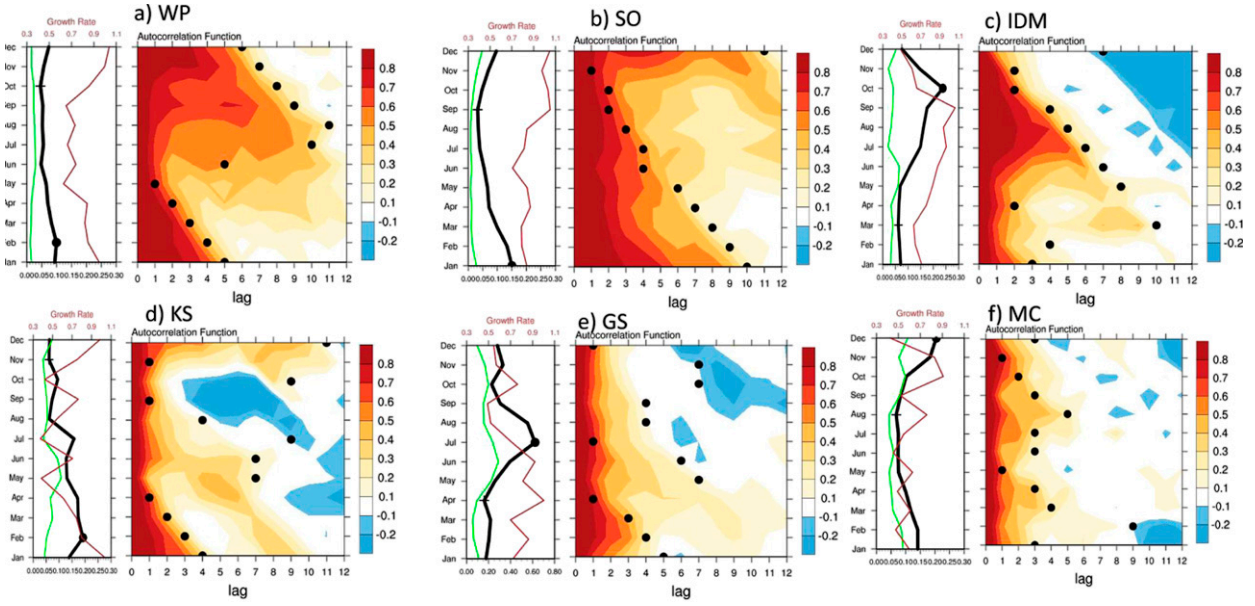

FIG. 9. In each panel, (right) the seasonal ACF map calculated directly from the observation and (left) the annual cycles of SST variance (black), lag-1 correlation coefficient (representing the growth rate) (brown), and the noise forcing variance (green) for the (a) western tropical North Pacific (WP; 10°–15°N, 130°–160°E), (b) Southern Ocean (SO; 45°–55°S, 150°–110°W), (c) Indian Ocean dipole mode defined as the SST difference between the eastern and western equatorial Indian Ocean (the two IDM boxes in Figs. 7a and 8e), (d) Kuroshio (KS; 22°–36°N, 122°–150°E), (e) Gulf Stream (GS; 40°–50°N, 60°–30°W), and (f) Malvinas Current (MC; 40°–50°S, 60°–30°W). These regions are marked in black boxes in both Figs. 7a and 8e.

tropical Indian Ocean. The IDM variance peaks in fall (Saji et al. 1999; left panel in Fig. 9c) and the ACF shows a PB locked to earlier in the year (Fig. 9c) ($\sigma_B = 3.5$, $\bar{t}_{B_0} = 3.5$, $S_{B_1} = 2.7$). Theoretical forcing parameters ($B = 0.73$, $A = 0.92$, $D = 0.15$, $\beta = -60°$) and individually forced solutions (not shown) suggest that the PB is forced overwhelmingly by the seasonal growth rate. The PB in IDM has been recognized to be contributed mainly by that in the eastern equatorial Indian Ocean and has been speculated to enable the climate signal in the tropical Pacific region to cross the spring PB of ENSO and then influence summer monsoon in Asia (e.g., Torrence and Webster 1998). Note that the large spread of PB month ($\sigma_B > 3$) is caused by the ACF gradient in boreal winter when the growth rate and variance are the minimum and therefore the ACF is sensitive to sampling error. Indeed, in both the solutions of the AR1 model and stochastic model, the PB is locked sharply to December (not shown).

There are also regions of large SST variance but no clear seasonal PB. This can be seen in the ACF of the Kuroshio (KS; 22°–36°N, 122°–150°E) ($\sigma_B = 3.8$, $\bar{t}_{B_0} = 7.4$, $S_{B_1} = 3.1$) and Gulf Stream (GS; 40°–50°N, 60°–30°W) ($\sigma_B = 3.8$, $\bar{t}_{B_0} = 6.7$, $S_{B_1} = 2.6$) regions (Figs. 9d, e), where the PB points are scattered around with a large spread ($\sigma_B > 3$). These two regions are on the margin of forcing threshold (Fig. 8g; see also Fig. B1) and are therefore sensitive to other minor factors, such as sampling errors, higher harmonics, and the phase difference between the growth rate and noise forcing. For example, in theory, in the KS region ($B = 1.24$, $A = 0.68$, $D = 0.32$, $\beta = 116°$), the growth rate alone is strong enough ($A > 1/2$) to generate a PB (in April), the noise forcing alone is too weak to overcome the strong damping ($D < B/2$) to generate a seasonal PB, and the combined forcing forces no PB, suggesting the dominant role of the noise forcing. Yet, in the AR1 solution, seasonal growth rate and the combined forcing both force a PB (in April; not shown) whereas the seasonal noise forcing forces no PB, suggesting a dominant role of growth rate forcing. The difference between the two models is likely caused by the higher harmonics, which are strong as seen in the growth rate and variance (left panel of Fig. 9d). In the GS region ($B = 1.08$, $A = 0.58$, $D = 0.5$, $\beta = 99°$), seasonal growth rate and the noise forcing are both barely strong enough to force a PB (in August and March, respectively, not shown). Yet, the combined forcing generates no PB. This occurs because the phase difference between the growth rate and noise forcing is $\beta \sim 90°$ and therefore the two forcing amplitudes tend to cancel each other on the combined forcing amplitude M in (2.14c). In the AR1 model solutions to both KS and GS regions, the combined forcing is still able to force a spring PB. This also suggests that the absence of a clear PB in both regions in the observation (Figs. 9d,e) may be caused by sampling errors. The sampling error is particularly effective in distorting the PB because of the strong damping and in turn the short persistence in these regions.

Finally, there are also widespread regions completely absent of seasonal PB, even with large SST variance, such as the region of Malvinas Current (MC; 40°–50°S, 60°–30°W). There is no seasonal PB in the ACF (Fig. 8f; $\sigma_B = 3.8$, $\bar{t}_{B0} = 7.8$; $S_{B_1} = 2.6$). Now, the theoretical forcing parameters ($B = 1.5$, $A = 0.27$, $D = 0.39$, $\beta = 59°$) are below the threshold for both the growth rate forcing and noise forcing. Neither the theory nor the AR1 model solution is able to generate a seasonal PB, regardless of a single forcing or combined forcing (not shown). The absence of the seasonal PB here is caused by the too weak seasonal forcing and too strong damping such that it is far below the threshold for PB (Figs. B1 and 8e).

In sum, clear seasonal PB can be identified in various regions of the World Ocean; these seasonal PBs are caused mainly by the seasonal growth rate in the tropics but by the seasonal noise forcing in the extratropics. These seasonal PBs can largely be understood in terms of our theory as the forcing magnitude exceeding the threshold. In some extratropical regions where forcing parameters are near the margin of the threshold, the seasonal PB either is absent or is generated/distorted by more subtle factors, such as sampling error and higher harmonics.

7. Conclusions and discussion

a. *Conclusions*

We have developed a theory for the seasonal PB in the simplest stochastic climate system in the Langevin equation. Our results can be summarized as addressing the three questions raised in the introduction.

First, what is the necessary forcing condition for a seasonal PB? A maximum decline of ACF, or PB, is generated when the magnitude of the seasonal forcing, in either growth rate or noise forcing, overwhelms the damping rate, such that the forcing/damping ratio exceeds a modest forcing threshold [$M/B > 1/2$ as in (2.19)]. Once generated, all the PBs are phase locked to the same calendar month [ωt_{B_0} in (2.23)], forming the so-called seasonal PB.

Second, what determines the timing and intensity of a seasonal PB? The season of the PB [ω_{B_0} in (2.23)] is determined by the decline of the seasonal forcing as well as the delayed response associated with the damping rate. For a weak damping and a strong seasonal forcing, the PB season is locked close to the month of minimum

SST variance under the growth rate forcing, but after the minimum SST variance under the noise forcing. The intensity of the PB is determined mainly by the amplitude of the seasonal forcing, with a stronger seasonal forcing generating a sharper PB [S_B or S_{B_1} in (2.25) and (2.26)].

Third, are there other regions in the World Ocean where seasonal PB is present and, if yes, why they are present? There are many regions where a seasonal PB is present, mainly because of the strong seasonal forcing. In the tropics, the seasonal PB tends to be forced by a strong seasonal growth rate, whereas in the extratropics the seasonal PB tends to be generated by a strong seasonal noise forcing. Consistent with the observation, our theory predicts seasonal PBs in some regions, such as the austral summer PB in the Southern Ocean and the spring PB in the western tropical Pacific.

Overall, our theory is able to predict most major features of the seasonal PB in the observation. Therefore, we suggest that this theory can serve as a null hypothesis for the seasonal PB of climate variability in general.

b. Discussion

Our theory suggests that a seasonally phase-locked PB is an intrinsic feature of a stochastic climate system with a moderate seasonal forcing. Given the applicability of the stochastic climate model to a wide range of climate variability (Hasselmann 1976; Penland and Magorian 1993), our theory may have implications for seasonal to interannual climate variability in general. Although the seasonal PB has been studied most intensively on the tropical Pacific ENSO, it may be applied to other regions and for other climate variables that exhibit significant seasonal modulations, such as sea ice variability (Moon and Wettlaufer 2011) and the seasonal thermocline (Alexander et al. 1999). In practice, however, the study of seasonal PB is more interesting for the case of weak damping, or longer persistence, because a strongly damped system leads to a rapid decline of ACF and therefore little predictability after the decorrelation time. Furthermore, since our theory may also have implications to a general stochastic climate system forced by a periodic forcing. For example, diurnal cycle is the other strong periodic forcing on the atmosphere and our theory in principle also applies to short-term weather prediction with diurnal cycle. Does the short-term weather forecast exhibit a predictability barrier phased locked to the diurnal cycle?

Much further work is needed to further improve our PB theory. First, we have focused on the annual harmonic here, while the full seasonal cycle in the observation often includes significant subannual higher harmonics. Therefore, the impact of higher harmonics and their interaction with the annual harmonic need to be further studied. Second, our theory is developed for the Langevin equation or AR1 model, while climate variability in some regions, such as the tropical Pacific ENSO, also exhibits significant oscillatory features that are better described in an oscillatory model or an AR2 system. Our current results show empirically that the AR1 model here severely underestimates the intensity of the PB. Therefore, to better assess the PB intensity, the seasonal PB theory should be developed further in an AR2 model or an oscillatory model (e.g., Stein et al. 2010; Levine and McPhaden 2015) and even multidimensional system (e.g., Penland and Magorian 1993).

Acknowledgments. We thank four anonymous reviewers for their comments on several versions of this paper. This work is supported by Chinese Ministry of Science and Technology Grant 2017YFA0603801, Natural Science Foundation of China Grant 41630527, and U.S. National Science Foundation Grant AGS-1656907.

APPENDIX A

Minimum ACF

The minimum autocorrelation function (ACF), which is sometimes referred to as the minimum persistence, has often been referred as a type of PB. We will show here, however, that, the minimum persistence differs dramatically from the maximum ACF decline. The minimum persistence always exists year round, with no forcing threshold. Moreover, the minimum persistence is not phase-locked to a particular calendar month and therefore does not form a "seasonal" barrier. In the ACF (2.14a), for a given τ, the minimum ACF during a year can be derived as

$$\partial_t r(t,\tau) = e^{-b_0\tau}\frac{\omega BM}{2\sqrt{1+B^2}}\sin\left(\frac{\omega\tau}{2}\right) \times\cos\left(\omega t+\frac{\omega}{2}\tau-\theta_1-\theta_3\right)=0. \quad \text{(A.1)}$$

The minimum persistence exists on the phase line

$$\omega t+\frac{\omega}{2}\tau-\theta_1-\theta_3=\pi \quad \text{(A.2)}$$

or

$$\omega t_p(\tau)=\omega t_{p_0}-\frac{\omega}{2}\tau, \quad \text{(A.3)}$$

with the initial month at $\tau=0$ as

$$\omega t_{p_0}=\theta_1+\theta_3+\pi. \quad \text{(A.4)}$$

In contrast to the maximum ACF decline, or PB, discussed in (2.22) and (2.23), the minimum persistence is present regardless of the magnitude of the seasonal forcing. Furthermore, the month of minimum persistence ωt decreases at half the rate of the lag $(\omega/2)\tau$. Therefore, the minimum persistence does not occur on the same calendar month, and therefore does not form a ''barrier'' on a fixed season. Instead, its calendar month is delayed by half a month away from ωt_{p_0} as the lag increases by one month. These features can be seen in the examples in Figs. 1a,c, 2a–c, and 4a–c.

In ENSO studies, sometimes the PB month has been thought to be equivalent to the minimum of lag-1 ACF (e.g., Torrence and Webster 1998). Our theory shows that this is not the case in general. Indeed, a comparison of ωt_{p_0} with the PB month ωt_{B_0} in (2.22) shows a difference as

$$\omega t_{B_0} - \omega t_{p_0} = \theta_1 + \theta_4 - \pi.$$

Nevertheless, in the case of weak damping and strong seasonal forcing, $\theta_1 \to \pi/2$ according to (2.10) and $\theta_4 \to \pi/2$ according to (2.21), such that the initial minimum persistence month ωt_{p_0} approaches the PB month ωt_{B_0}. These features of the minimum persistence can be seen in the tropical and North Pacific (Fig. 1), and the solutions to the Langevin equation in Figs. 2 and 4, and will be discussed in more detail in a companion paper (Y. Jin et al. 2018, unpublished manuscript).

For a decreasing month t, the lag of maximum ACF decline τ_B increases as $-t$ in (2.20); the lag of minimum ACF τ_P, however, increases twice the rate as $-2t$ in (A.2), so that $\tau_P \sim 2\tau_B$. This can be understood roughly as follows. The lag of maximum ACF decline τ_B can be estimated as the gradient between the initial ACF $r(t,0) = 1$ and the minimum ACF $r(t, \tau_P)$ in the central-difference scheme as

$$\frac{\partial r}{\partial \tau}(t, \tau_B) \approx \frac{r(t, 2\tau_B) - r(t,0)}{2\tau_B} = \frac{r(t, \tau_P) - 1}{2\tau_B}.$$

APPENDIX B

Comparison of the Asymptotic Solution with the Full Solution

The asymptotic solutions for seasonal PB in (2.19) and (2.22) are derived in the regime of weak seasonal forcing and weak damping under the assumption of (2.8), (2.13), and (2.15). Yet, as in the cases of many other asymptotic solutions, this asymptotic solution holds reasonably well in a parameter regime broader than the formal assumption. Here, the asymptotic solution is largely valid up to $B \sim 1$. This can be seen by comparing the asymptotic solution with the full solution of (2.6) and (2.7) in Figs. B1a and B1b (black circles). The forcing threshold under the seasonal growth rate in (3.1) is compared with the full solution in Fig. B1a in a set of experiments of varying B and A. It is seen that the threshold amplitude A is generally indeed close to the threshold 1/2 derived from the asymptotic solution. When B increases beyond 1, the threshold amplitude starts to exceed 1/2 modestly. This suggests that the asymptotic threshold $A = 1/2$ is an underestimation of ~10%–20% for large values of B. Similarly, under the seasonal noise forcing, Fig. B1b shows that the threshold $D = B/2$ in (4.1) is also a good approximation to the full solution. Opposite to the growth rate case in Fig. B1a, however, at large B, the threshold becomes smaller than the asymptotic threshold, so the latter has a modest overestimation of 10%–20%.

The threshold can also be seen consistent with the eight regions discussed in Fig. 1 (ENSO and NP) and Fig. 9 (WP, SO, IDM, KS, GS, and MC), which are shown in cyan circles in Fig. B1a (Fig. B1b) when forced by the seasonal growth rate (noise forcing) alone. Solid and hollow circles represent the presence and absence of a seasonal PB, respectively. In addition, a red plus sign indicates the presence of seasonal PB when forced by the combined growth rate and noise forcing. In some regions, the seasonal PB forced by the combined forcing shows some difference from that under the single forcing because of the interference between the two forcing. For example, NP has a seasonal PB in Fig. B1a even though its seasonal growth rate A is well below the threshold; the IDM has a seasonal PB in Fig. B1b even though the seasonal noise forcing D is well below the threshold, because of the interference between the two forcing.

Figure B2 also shows that the PB month and intensity, as functions of the magnitude of seasonal forcing, compare well between the asymptotic solution and the full solution. Two cases are shown, one weak damping $B = 0.2$ (black) and the other strong damping $B = 0.6$ (red). For the growth rate forcing, under a weak damping, the seasonal PB emerges (black solid) only after A exceeds 0.6, consistent with the forcing threshold $A = 1/2$ (Fig. B2a). The PB month ωt_{B_0} increases rapidly from month −6 at $A \sim 0.5$ to a saturation month at around month −4 toward $A \sim\sim 2$. This full solution is well approximated by the asymptotic solution (3.2) even for a large amplitude of A up to 6 (black dot). For very large A, the PB month saturates toward $\omega t_{B_0} = -4$,

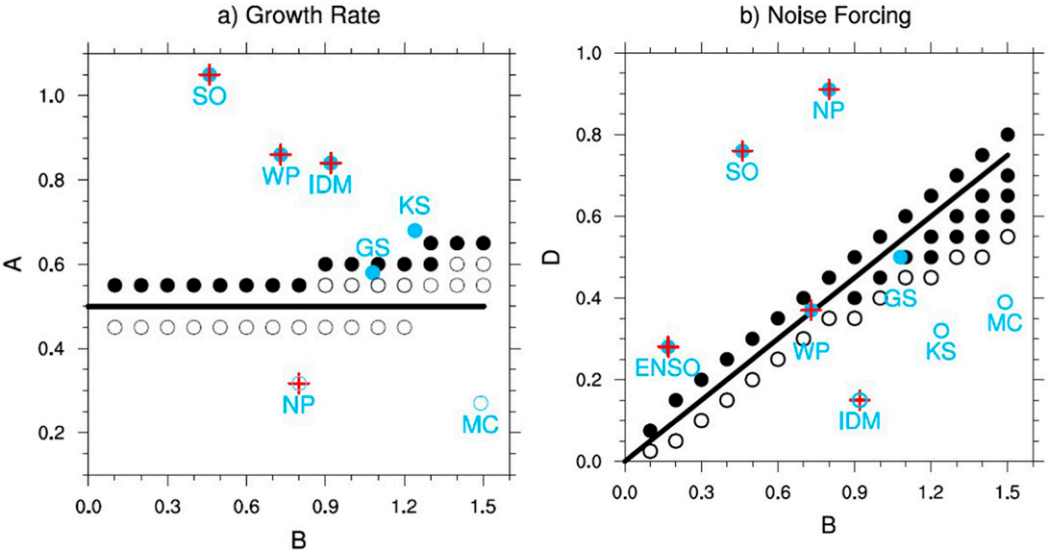

FIG. B1. Sensitivity experiments testing the seasonal PB around the forcing threshold for different damping rates B in the full theoretical solution. (a) Black circles represent the experiments forced by the seasonal growth rate only ($D = 0$); a black filled (hollow) circle represents the parameter pair (B, A) where a seasonal PB is (is not) present. The heavy line is the forcing threshold from the leading-order solution as $A = 1/2$. (b) Black circles represent the solution forced by the seasonal noise forcing only ($A = 0$); a black filled (hollow) circle represents the parameter pair (B, D) where a seasonal PB is (is not) present. The heavy line is the forcing threshold from the leading order solution $D = B/2$. It is seen that the leading-order solution holds well up to $B \sim 1$. For $B > 0.8$, the asymptotic solution underestimates the threshold for growth-rate forcing, but overestimates the threshold for noise forcing, modestly. In addition, gray circles represent the parameter pairs of the eight regions discussed in Fig. 1 (ENSO, NP), and Fig. 9 (WP, SO, IDM, KS, GS, and MC); a filled (hollow) circle represents the case where the seasonal PB is (is not) present, forced by (a) the seasonal growth rate only ($D = 0$) and (b) the seasonal noise forcing ($A = 0$) only. A red plus sign represents the case where the combined forcing forces a seasonal PB. The ENSO case is missing in (a) because the amplitude A is beyond the scale.

which leads the minimum variance at $\omega t_V = -3.4$ (black dashed) by -0.6 months in the full solution. For the case of strong damping, the full solution also shows a PB emerging after $A > 0.6$ and the PB month increasing with A, except now the PB month is shifted earlier by about a month (red solid). This overall change of the PB month is also approximately by the leading-order solution (red dot), although the error is somewhat larger, because of the larger B.

The total intensity of the PB in the full solution increases almost linearly with A in the full solution (black and red solid lines) (Fig. B2b). This change is approximated by the asymptotic solution (3.6) well for the case $B = 0.2$ (black dot) and also reasonably well for the case of $B = 0.6$ (red dot). Overall, all the major features of the seasonal PB are in good agreement with the asymptotic solution. The PB month and intensity of the seasonal PB in response to seasonal noise forcing can be discussed similarly as shown in Figs. B2c and B2d. Note that now the seasonal PB emerges at increasing values of D for increasing B, consistent with the asymptotic threshold $D = B/2$ in (4.1).

APPENDIX C

Methods for Constructing ACF from the Monthly Observation

Five methods are used for the construction of the ACFs for the analysis of seasonal PB from the monthly SST observation.

a. Method 1: Direct observational calculation

The SST anomaly T_t is derived after removing the climatological seasonal cycle such that the mean of SST anomaly for each calendar month is zero. Here, the time index $t = 12n + m$ is in month, with n as the year and m as the calendar month. The autocorrelation function (ACF) for calendar month m and lag k is calculated as

$$r(m,k) = \frac{\sigma^2_{m,m+k}}{\sigma^2_m}, \tag{C.1}$$

where the covariance and variance for the calendar month m are

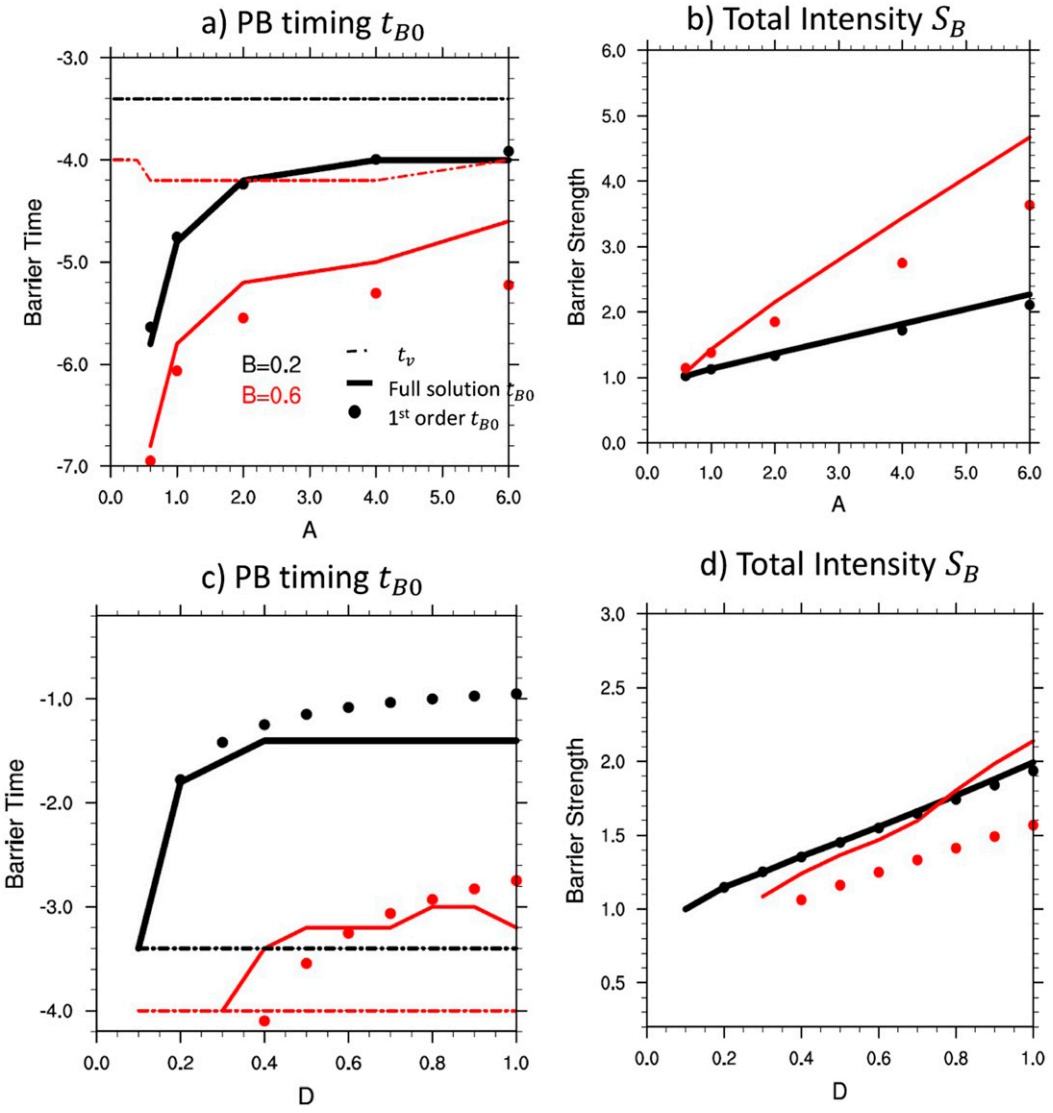

FIG. B2. (a),(c) PB month ωt_B and (b),(d) total PB intensity S_B as functions of the amplitude of the seasonal (top) growth rate and (bottom) noise forcing for the damping rates of $B = 0.2$ (black) and $B = 0.6$ (red). The full solutions are in heavy solid lines, and the leading order solutions are in solid circles. The minimum variance month ωt_V is shown in dashes.

$$\sigma^2_{m,m+k} = \frac{1}{N-1}\sum_{n=0}^{N-1} T_{12n+m} T_{12n+m+k}, \qquad \text{(C.2)}$$

$$\sigma^2_m \equiv \sigma^2_{m,m}, \qquad \text{(C.3)}$$

with $N = 46$ being the total years. All the calendar month indices here are periodic as

$$\langle\cdot\rangle_{m+12} = \langle\cdot\rangle_m.$$

b. *Method 2: AR1 model solution*

Assume the observation can be modeled as an AR1 process

$$X_t = a_m X_{t-1} + \varepsilon_t, \qquad \text{(C.4)}$$

where $a_m = r(m, 1)$ is the lag-1 ACF derived in (C.1). The term ε_t can be calculated as the residual of the observation time series: $\varepsilon_t = T_t - a_m T_{t-1}$, and can be treated as a random noise of zero mean. The variance of the noise of month m is calculated as

$$\sigma^2_{\varepsilon,m} = \frac{1}{N-1}\sum_{n=0}^{N-1} \varepsilon_{12n+m}\varepsilon_{12n+m}. \qquad \text{(C.5)}$$

The SST variance in the AR1 model forced by seasonal growth rate and noise forcing can be calculated as [(A6) of Torrence and Webster (1998)]

$$\sigma_m^2 = \frac{\sigma_{\varepsilon,m}^2 + \sigma_{\varepsilon,m-1}^2 a_m^2 + \sigma_{\varepsilon,m-2}^2 a_m^2 a_{m-1}^2 + \cdots + \sigma_{\varepsilon,m-11}^2 \prod_{j=0}^{10} a_{m-j}^2}{1 - \left(\prod_{j=1}^{12} a_j\right)^2}. \tag{C.6}$$

The ACF of the AR1 model can then be calculated as [(A9) of Torrence and Webster (1998)]

$$r^{\mathrm{AR1}}(m,k) = \frac{\sigma_m}{\sigma_{m+k}} \prod_{j=1}^{k} a_{m+j}. \tag{C.7}$$

In the case of seasonal growth rate forcing only, the noise variance $\sigma_{\varepsilon,m}^2$ in (C.6) is replaced by its annual mean, and in the case of seasonal noise only, the lag-1 coefficient a_m in (C.6) and (C.7) are replaced by its annual mean.

c. *Method 3: Full solution to the Langevin equation*

We fit the monthly SST to the seasonal Langevin equations [(2.1)–(2.3)] by estimating the model parameters. The seasonal Langevin equation [(2.1)] is discretized in the time step of $\Delta t = 1$ month as

$$X_{t+1} = (1 - b_m)X_t + N_t, \tag{C.8}$$

similar to Moon and Wettlaufer (2017). A comparison of (C.8) and (C.4) shows that the seasonal cycle of the growth rate and noise variance can be derived as $b_m = 1 - a_m$ (in month^{-1}), and $\sigma_{N,m}^2 = \sigma_{\varepsilon,m}^2$. We then obtain A, D, b_0, σ_0^2, and $\beta(=\theta_A - \theta_D)$ from the least squares fit of the 12 monthly values of the seasonal growth rate b_m and variance of the seasonal noise forcing $\sigma_{N,m}^2$ to the annual harmonic function of $b_0[1 - A\cos(\omega t + \theta_A)]$ and $\sigma_0^2[1 + D\cos(\omega t + \theta_D)]$, respectively, where $\omega = \pi/(6\ \text{months})$. With these model parameters, the full solution of the Langevin equation can be obtained by the numerical integration of the covariance function (2.4) and then in the ACF (2.7).

d. *Method 4: Asymptotic solution to the Langevin equation*

To understand the seasonal PB qualitatively, an ACF is derived from the asymptotic solution of the seasonal Langevin equation in the limit of weak seasonal forcing and weak damping ($B \ll 1$, $BA \ll 1$, $BD \ll 1$) using the analytical solution of the ACF (2.18).

e. *Method 5: AR2 model simulation*

The observation is also assessed in section 6 with the second-order autoregressive (AR2) model in the form of

$$X_t = a_m X_{t-1} + c_m X_{t-2} + \eta_t, \tag{C.9}$$

where $a_m = P_m(1)$ and $c_m = P_m(2)$ are the lag-1 and lag-2 auto-regression coefficients for month m derived in (C.1). The residual noise is calculated with the observational time series as

$$\eta_t = T_t - a_m T_{t-1} - c_m T_{t-2}. \tag{C.10}$$

The seasonal cycle of the noise variance $\sigma_{\eta,m}^2$ is then calculated as

$$\sigma_{\eta,m}^2 = \frac{1}{N-1} \sum_{n=0}^{N-1} \eta_{12n+m}\eta_{12n+m}.$$

The AR2 model [(C.9)] is then simulated 20 times, each with a realization of a Gaussian white noise of the seasonal variance $\sigma_{\eta,m}^2$. The 20 members are ensemble averaged first to reduce sampling error and the ensemble mean time series is then used to calculate the ACF for AR2 model.

REFERENCES

Alexander, M. A., C. Deser, and M. S. Timlin, 1999: The reemergence of SST anomalies in the North Pacific Ocean. *J. Climate*, **12**, 2419–2433, https://doi.org/10.1175/1520-0442(1999)012<2419:TROSAI>2.0.CO;2.

Bennett, W. R., 1958: Statistics of regenerative digital transmission. *Bell Syst. Tech. J.*, **37**, 1501–1542, https://doi.org/10.1002/j.1538-7305.1958.tb01560.x.

Boschat, G., P. Terray, and S. Masson, 2013: Extratropical forcing on ENSO. *Geophys. Res. Lett.*, **40**, 1605–1611, https://doi.org/10.1002/grl.50229.

Hasselmann, K., 1976: Stochastic climate models. Part I: Theory. *Tellus*, **28**, 473–485, https://doi.org/10.3402/tellusa.v28i6.11316.

——, and T. P. Barnett, 1981: Techniques for linear prediction for systems with periodic statistics. *J. Atmos. Sci.*, **38**, 2275–2283, https://doi.org/10.1175/1520-0469(1981)038<2275:TOLPFS>2.0.CO;2.

Hurd, H. L., 1975: Periodically correlated processes with discontinuous correlation functions. *Theory Probab. Appl.*, **19**, 804–807, https://doi.org/10.1137/1119088.

Jin, F., S. T. Kim, and L. Bejarano, 2006: A coupled-stability index of ENSO. *Geophys. Res. Lett.*, **33**, L23708, https://doi.org/10.1029/2006GL027221.

Levine, A. F. Z., and M. J. McPhaden, 2015: The annual cycle in ENSO growth rate as a cause of the spring predictability barrier. *Geophys. Res. Lett.*, **42**, 5034–5041, https://doi.org/10.1002/2015GL064309.

Moon, W., and J. S. Wettlaufer, 2011: A low-order theory of Arctic sea ice stability. *Europhys. Lett.*, **96**, 39001, https://doi.org/10.1209/0295-5075/96/39001.

——, and ——, 2017: A unified nonlinear stochastic time series analysis for climate science. *Sci. Rep.*, **7**, 44228, https://doi.org/10.1038/srep44228.

Penland, C., and T. Magorian, 1993: Prediction of Nino 3 sea surface temperatures using linear inverse modeling. *J. Climate*, **6**, 1067–1076, https://doi.org/10.1175/1520-0442(1993)006<1067:PONSST>2.0.CO;2.

Rayner, N. A., D. E. Parker, E. B. Horton, C. K. Folland, L. V. Alexander, D. P. Rowell, E. C. Kent, and A. Kaplan, 2003: Global analyses of sea surface temperature, sea ice, and night marine air temperature since the late nineteenth century. *J. Geophys. Res.*, **108**, 4407, https://doi.org/10.1029/2002JD002670.

Ren, H. L., F. F. Jin, B. Tian, and A. A. Scaife, 2016: Distinct persistence barriers in two types of ENSO. *Geophys. Res. Lett.*, **43**, 10 973–10 979, https://doi.org/10.1002/2016GL071015.

Ruiz de Elvira, A., and P. Lemke, 1982: A Langevin equation for stochastic climate models with periodic feedback and forcing variance. *Tellus*, **34**, 313–320, https://doi.org/10.3402/tellusa.v34i4.10818.

Saji, N. H., B. N. Goswami, P. N. Vinayachandran, and T. Yamagata, 1999: A dipole mode in the tropical Indian Ocean. *Nature*, **401**, 360–363, https://doi.org/10.1038/43854.

Stein, K., N. Schneider, A. Timmermann, and F.-F. Jin, 2010: Seasonal synchronization of ENSO events in a linear stochastic model. *J. Climate*, **23**, 5629–5643, https://doi.org/10.1175/2010JCLI3292.1.

Tasambay-Salazar, M., M. J. Ortizbevia, F. J. Avarez-Garcla, and A. M. Ruiz De Elvira, 2015: The Nino3.4 region predictability beyond the persistence barrier. *Tellus*, **67A**, 27457, https://doi.org/10.3402/tellusa.v67.27457.

Torrence, C., and P. J. Webster, 1998: The annual cycle of persistence in the El Niño/Southern Oscillation. *Quart. J. Roy. Meteor. Soc.*, **124**, 1985–2004, https://doi.org/10.1002/qj.49712455010.

Troup, A. J., 1965: The 'southern oscillation.' *Quart. J. Roy. Meteor. Soc.*, **91**, 490–506, https://doi.org/10.1002/qj.49709139009.

Walker, G. T., and E. W. Bliss, 1932: World Weather V. *Mem. Roy. Meteor. Soc*, **4** (36), 53–84.

Webster, P., and S. Yang, 1992: Monsoon and ENSO: Selectively interactive systems. *Quart. J. Roy. Meteor. Soc.*, **118**, 877–926, https://doi.org/10.1002/qj.49711850705.

Wright, P. B., 1979: Persistence of rainfall anomalies in the central Pacific. *Nature*, **277**, 371–374, https://doi.org/10.1038/277371a0.

Xue, Y., M. Cane, S. Zebiak, and M. Blumenthal, 1994: On the prediction of ENSO: A study with a low-order Markov model. *Tellus*, **46A**, 512–528, https://doi.org/10.3402/tellusa.v46i4.15641.

Zhao, X., J. Li, and W. Zhang, 2012: Summer persistence barrier of sea surface temperature anomalies in the central western North Pacific. *Adv. Atmos. Sci.*, **29**, 1159–1173, https://doi.org/10.1007/s00376-012-1253-2.